Supplementary Information for
The Ras Dimer Structure

Till Rudack[1,2,*,#], Christian Teuber[1,2,*], Marvin Scherlo[1,2], Jörn Güldenhaupt[1,2], Jonas Schartner[2], Mathias Lübben[1,2], Johann Klare[3], Klaus Gerwert[1,2,#], Carsten Kötting[1,2,#]

[1] Biospectroscopy, Center for Protein Diagnostics, Ruhr University Bochum, 44801 Bochum, Germany
[2] Department of Biophysics, Ruhr University Bochum, 44801 Bochum, Germany
[3] Department of Physics, Osnabrück University, 49074 Osnabrück, Germany

* These authors contributed equally to this work

[#] Corresponding author

Till.Rudack@ruhr-uni-bochum.de
Klaus.Gerwert@ruhr-uni-bochum.de
Carsten.Koetting@ruhr-uni-bochum.de

Table of Contents

Supporting Note 1: Ras dimer structural models available in the literature

The literature reports various different contradictory dimer structural models.[1–4] We categorize these models into three main categories based on their dimer interaction sides. The models in category I undergo helix α4 and α5 dimerization, the ones in category II undergo helix α3 and α4 dimerization, while the ones in category III undergo β-sheet dimerization. These categories are further subdivided with respect to their detailed dimer interactions in Fig. S1. Structure I.1 is the protein-protein crystal contact interface that is most prominent among all available Ras X-ray structures.[1] However, several other different protein-protein contact interfaces occur in the deposited X-ray structures. Using biomolecular simulations for N-Ras and a combination of biomolecular simulations and protein docking (RosettaDock[5]) for K-Ras4B, the model I.2 for N-Ras-GDP[1] and two models for K-Ras4B-GTP[4] were obtained, respectively. One of the two K-Ras4B-GTP models has the same contact side as model I.2, and the other one is referred to as model II.1.[4] Model I.3[2] is the first model deposited under the protein data bank (PDB) ID 6W4F, which was obtained by utilizing high ambiguity driven protein−protein docking (HADDOCK) with NMR derived distance restraints of K-Ras4B-GDP attached to a nanodisc.[2] Using the same methods, the authors also published a K-Ras4B-GTP-ɣ-S structure (PDB-ID: 6W4E) referred to as model I.4. Models II.2 (K-Ras4B-GppNHp) and III.1 (K-Ras4B-GTP-ɣ-S)[3] were generated by the protein interactions by structural matching (PRISM) algorithm.[6]

Supporting Note 2: Protein-Protein Docking

We constructed seven representative Ras monomer G-domains (residue 1 to 172) as input structures for the protein-protein docking servers. One representative model for each isoform (H-Ras, K-Ras4B and N-Ras) of the active conformation with a bound GTP analogon and the inactive conformation with GDP bound (two GDP bound models for H-Ras). As an initial starting point, the monomeric Ras structures from the protein data bank shown in Table S11 were used. Missing atoms and residues were completed using Modeller 9.21.[7] To achieve consistency and minimize the effect of crystallization artifacts due to different C-terminal truncation positions we modeled the C-terminal part helical until residue 172. The assumption that helix α5 ends approximately at residue 172 is in agreement with FTIR measurements [8] and NMR studies.[9, 10]
The resulting structures were sent to the PRISM[6,11], ZDOCK[12] and Symmdock[13,14] docking servers. Table S1 summarizes the resulting 178 dimer structural models, which are categorized based on their interaction sides into 9 main categories. While three of these interaction sides were already identified in the published models, six new interaction sides were detected (IV-IX). The dimer models are categorized as follows: I (contact between the surfaces formed by helices α4 and α5), II (contact between the surfaces formed by helices α3 and α4), III (contact between the surfaces formed by the β-sheets), IV (contact between helices α3 and α4 of one monomer with the β-sheet of the other monomer), V (contact between the helices α4 and α5 of one monomer with the β-sheet of the other monomer), VI (contact between the surfaces formed by helices α5 and the α-sheet), VII (contact between the surfaces formed by helices α4), VIII (contact between the surfaces formed by the helices α2 and α5), IX (involvement of the switch regions of at least one monomer in the dimer interface). Due to the huge variety of predicted dimer models a satisfactory validation of a distinct structural model is impossible without further experimental data. The main categories are further divided into 64 subcategories to distinguish detailed differences in the interaction pattern.

Supporting Note 3: Preparation of lipidated N-Ras with site specific fluorescence label

Lipid Anchor Synthesis for N-Ras

The organic synthesis of the lipid anchor Maleimidocaproyl-Gly-Cys(Hexadecyl)-Met-Gly-Leu-Pro-Cys(Farnesyl)-OMethyl was done based on Bader et al.[15] Synthesis of Fmoc-Cys(Farnesyl)-OH (Fig. S10A): In a 100 mL flask 690.61 mg L-cysteine (5.7 mmol) was dissolved in methanol under an argon atmosphere (11 mL) and cooled in an ice bath to 0 °C. The solution was stirred and 7 N ammonia in methanol (15 mL) were added slowly. Farnesyl bromide (1545.6 µL, 5.7 mmol) was added and the mixture was stirred for 3 h at 0 °C and 1 h at room temperature. Subsequently, the solvent was evaporated under reduced pressure. The remaining white solid was transferred into a 50 mL falcon tube and washed with n-pentane. The pentane suspension was centrifuged for 10 min (4500 rpm) and the supernatant was disposed. This procedure was repeated three times to get rid of unbound farnesyl bromide. The residue was placed in a round bottom flask and dichloromethane was added (50 mL). The resulting suspension was cooled to 0 °C and 880 µL triethylamine (6.28 mmol), 2.12 g Fmoc N-hydroxysuccinimide ester (6.28mmol) were added. The reaction mixture was stirred over night at room temperature. The suspension was filtrated to get rid of free Fmoc and the solvent was evaporated under reduced pressure. Purification was done by column chromatography using a gradient of 0-4% methanol in dichloromethane (DCM). Identification of the fractions was done by thin layer chromatography (Rf(product)=0.55, Rf(Fmoc)=0.9, 10% methanol in DCM). The product was a slightly yellow oil (yield 3.1 g, 98%), which was characterized by 1H-NMR.

Synthesis of Fmoc-Cys(Hexadecyl)-OH (Fig. S10B): 5 g of Fmoc-Cys(Trityl)-OH were dissolved in DCM (125 mL) in a round-bottom flask filled with argon. To the stirred solution 5 mL of trifluoroacetic acid and 3.75 mL of triethylsilane were added and allowed to react for 4 h at room temperature. Toluene was added (30 mL) and the crude product was coevaporated three times. Afterward, the crude product was transferred into a falcon tube and n-pentane was added. The tube was placed into a sonicator to mix the solution. By centrifugation the product (Fmoc-Cys-OH) was separated and the process was repeated three times.

To get rid of the oxygen, DCM was purged with argon for 30 min in a sonicator. The obtained 2.9 g of Fmoc-Cys-OH were dissolved in DCM (30 mL) and 7.8 mL hexadecane / 698 mg azobisisobutyronitrile (AIBN) were added. The mixture was refluxed at 85 °C for 3 h. Subsequently, the mixture cooled to room temperature and the solvent was removed with a rotating evaporator. The final product was purified using flash chromatography (silica gel) with a gradient of 0-4% methanol in DCM. The fractions containing the product were determined with TLC. The synthesis yielded in 3.4 g (72%) and the product was characterized by ^{1}H-NMR.

Activation and Loading of 2-Chlortritylchloride Resin: The 2-chlortritylchloride resin (800 mg, loading 0.77 mmol/g) was activated by adding 1.5 equivalent of thionyl chloride in 10 mL DCM. The mixture was stirred for 1 h at room temperature. Afterward, the resin was washed three times with DCM to get rid of the thionyl chloride. The resin and the Fmoc-Cys-OH were dried in vacuum overnight. Subsequently, the resin was dissolved in 7 mL DCM and mixed for 30 min under inert gas. After the addition of 1 g Fmoc-Cys-OH and 630 uL N,N-Diisopropylethylamine in 5 mL DCM to the activated resin the mixture was shaken for 3 h. The synthesis was done in a 0.25 mM scale with 320 mg of total resin. The loaded resin was divided into two equal parts. One part was immediately stored at -20°C under argon and the other one was used for the coupling in the solid phase peptide synthesis (SPPS).

Solid Phase Peptide Synthesis and Purification: The peptide sequence (Maleimidocaproyl-Gly-Cys(Hexadecyl)-Met-Gly-Leu-Pro-Cys(Farnesyl)-OMethyl) was synthesized with an automated solid-phase peptide synthesizer. For the SPPS 160 mg resin were employed. The cleavage of the peptide from the resin was done in a syringe. The resin was washed four times with DCM (20 mL). Subsequently, the resin was mixed with 1% trifluoroacetic acid (TFA) and 2% triethylsilane (TIS) in DCM for 30 min. This procedure was repeated three times to ensure a complete separation. After washing with DCM, the solvent was removed in rotating evaporator and three times coevaporated with toluene (10 mL). The yield of the crude peptide was 125 mg (95%). The crude peptide was purified using a preparative HPLC with a diphenyl-column (Vydac, Columbia, USA) and an acetonitrile gradient (50%→100%, 15 min, 0.08% TFA). After purification 93 mg (74%) of the desired peptide with lipid anchor were obtained.

Methylation of the Lipid Anchor (Fig. S11C): The last synthesis step was the methylation of the Cys(Far). Under an argon atmosphere 15 mg of the anchor were dissolved in toluene/methanol (9:1) and 0.9 equivalents of trimethylsilyldiazomethane ($TMSCHN_2$) were added. The mixture was stirred for 30 min and the solvent was evaporated.

The product was dissolved in dichloromethane and purified on a silica column with dichloromethane/methanol (97:3) as solvent. The fractions were characterized with ESI-MS. The product fractions were pooled and concentrated. The yield was 9.5 mg (63%). The product was characterized with ESI-MS 1316 g/mol $[M+H]^+$ and 1338 g/mol $[M+Na]^+$. The ESI-Spectrum of the final product is presented in Fig. S11D. The complete structure of the synthesized peptide Maleimidocaproyl-Gly-Cys(Hexadecyl)-Met-Gly-Leu-Pro-Cys(Farnesyl)-OMethyl is shown in Fig. S11E.

Finding suitable labeling sites

In order to find suitable labeling sites for the fluorophores or the spin-label, we performed expression experiments in *E.coli*. Therefore, 50 ml *E.coli* cultures were incubated and mixed with the unnatural amino acid as described below. Afterwards, the cells were disrupted and the homogenate, the supernatant as well as the pellet was tested for N-Ras (1-181) content via Western-Blot analysis with an antibody against the N-Ras C-terminus. Fig. S1 shows that N-Ras K88TAG, S106TAG and T124TAG exhibit more N-Ras in the supernatant as N-Ras V109TAG, D126TAG and P121TAG. In order to label opposing sites from N-Ras, we have finally chosen S106 and T124 as labelling sites (Fig. 2D).

Preparation of semisynthetic lipidated N-Ras protein with unnatural amino acids

We used a human N-Ras gene (amino acids 1-181) cloned in a pBAD-Vector in such a way that the complementary amino acid regions to H-Ras have been replaced by the human H-Ras codon in order to maximize the protein yield. The N-Ras protein was expressed in *E.coli* BL21 AI cells from Thermo Fisher Scientific (Waltham, MA, USA) with site specifically incorporated unnatural amino acids (UAAs) by the amber suppression strategy . Therefore, two plasmids were used: 1) pBAD_N-Ras1-181_S106TAG/T124TAG _±_C118S/E49Q_S106TAG_C118S_D154N for N-Ras and 2) a plasmid encoding $tRNA^{Pyl}/PylRS^{WT/AF}$ obtained from the Lemke group[16] for the incorporation of the unnatural amino acid N-Propargyl-L-Lysine (PrK; $PylRS^{WT}$) or Cyclooctyne-Lysine (SCO; $PylRS^{AF}$) from SiChem GmbH (Bremen, Germany).[16, 17] The C118S mutation was introduced to prevent the lipid anchor from binding to this position. The serine was chosen as a substitution for cysteine to keep potential side effects as small as possible. The cells were transfected with these two plasmids and a 50 ml LB-medium culture with 20 µg/ml Chloramphenicol (Cm), 50 µg/ml Ampicillin (Amp) was incubated at 37 °C overnight. The next day, a 4 Liter TB-medium culture with 20 µg/ml Cm, 50 µg/ml Amp was inoculated with a starting

OD_{600} = 0.05. The culture was incubated at 37 °C until an OD_{600} = 0.2 – 0.4 was reached. The unnatural amino acid with a concentration of 100 mM in 0.2 M NaOH, 15% (v/v) DMSO, diluted 1:4 with 1 M HEPES was added to the cells for a 1 mM final concentration of unnatural amino acid in the culture. The overnight protein expression at 30 °C was induced with 0.02% (w/v) arabinose (Sigma-Aldrich, St. Louis, MO, USA) at an OD_{600} = 0.6 – 0.8. The cells were harvested via centrifugation at 5000 g and resuspended in buffer (30 mM Tris (pH 7.5), 5 mM $MgCl_2$, 5 mM DTT, and 20 µM GDP). The cells were disrupted through microfluidization and N-Ras was isolated by anion exchange chromatography and size exclusion chromatography. The coupling of the lipid anchor at position C181 via a maleimide-group was modified based on a previously mentioned protocol.[18]

Coupling of N-Ras with the Lipid Anchor: The lipid anchor was used in a large excess (6 mg, 4.47 µmol) and was dissolved in 80 µL methanol. Subsequently, 7 mg of N-Ras (0.35 µmol) were added in a buffer containing 5% 3-[(3-Cholamidopropyl)dimethylammonio]-1-propanesulfonate (CHAPS) and 4% Triton X-100 (50 mM Tris, pH 7.4, 100 mM NaCl, 2 mM $MgCl_2$). The mixture was stirred at 4 °C for 16 h. The purification was done by gelfiltration using a buffer with 0.4 % Triton X-100. Afterwards the buffer was exchanged to a detergent free buffer (50 mM Hepes pH 7,4, 50 mM NaCl, 2 mM MgCl2, 20 µM GDP). To completely remove residual detergent, a Pierce Detergent Removal Spin Column (Thermo Fisher, Rockford, IL, USA) was applied. The yield was usually around 25%. The lipidated proteins were analyzed by MALDI or SDS-PAGE (Fig. S12).

To check whether the lipid anchor (MW = 1316 Da) is coupled to the protein, we analyzed the unmodified and the modified protein fraction using MALDI mass spectrometry or SDS-PAGE. The latter was performed if the samples could not be ionized, as it was the case with N-Ras T124PrK C118S and N-Ras E49Q S106PrK C118S D154N. Fig. S12A shows the MALDI mass spectrometry results for N-Ras WT and the mutant N-Ras S106PrK before and after lipidation. The mass differences of 1324 Da (N-Ras WT) and 1314 Da (N-Ras S106PrK) show, that the lipid coupling was successful. Fig. S12B shows the SDS-PAGE results for N-Ras T124PrK C118S and N-Ras E49Q S106PrK C118S D154N before and after lipid coupling. It is observed that the protein fractions “+ lipid anchor” have a larger mass in comparison to the unmodified protein “- lipid anchor”. Thus SDS page is used to determine the lipid coupling efficiency.

POPC liposome preparation

POPC was dissolved in chloroform at a concentration of 15 mg/ml. The $CHCl_3$ was evaporated using a nitrogen stream followed by incubation in vacuum (20 mbar) for 1 h. The lipid was then resuspended with buffer (50 mM Hepes (pH 7.5), 50 mM NaCl, 2 mM $MgCl_2$, and 20 µM GDP) to a final concentration of 50 mM. The POPC suspension was extruded (20 times, 400 nm filter). The size of the generated liposomes was checked by dynamic light scattering.

Coupling of fluorophores

For the time correlated single photon counting (TCSPC) experiments, the FRET-pair Atto 532 azide (donor)/Atto 655 azide (acceptor) from ATTO-TEC GmbH (Siegen, Germany) was site specifically coupled to the positions 106 and 124 of the N-Ras protein, respectively. For this purpose we used the copper (I) catalyzed azide-alkyne cycloaddition leading to 1,4-disubstituted 1,2,3-triazoles.[19] The final concentrations used are summarized in Table S9.

First $CuSO_4$ (final concentration: 0.1 mM) was mixed with the ligand Tris(3-hydroxypropyltriazolylmethyl)amine (THPTA) from Lumiprobe GmbH (Hannover, Germany) (final concentration: 0.5 mM). Next, the copper (II) ions were reduced to copper (I) with sodium ascorbate (final concentration: 2.5 mM), the solution has to appear colorless. Further, benzoic acid (final concentration: 20 µM)[20] as well as the protein with the unnatural amino acid PrK (final concentration: 24 µM) and the fluorophore (final concentration: 1 mM) were added. Buffer (50 mM

Hepes (pH 7.5), 50 mM NaCl, 2 mM $MgCl_2$, and 20 µM GDP) was added to the solution to a final volume of 100 µl. The unreacted fluorophore molecules were removed after incubation (31 °C, 2 h) using 4-5 Zeba™ Spin Desalting Columns (0.5 ml, 7 kDa cutoff) from Thermo Fisher Scientific until no more dyes were present in the throughflow. The labeling efficiencies were determined by the ratio of the fluorophore and protein concentration. The coupling efficiencies are also summarized in Table S10.

Coupling of the spin label Azido-Proxyl

Purified and lipidated N-Ras T124-SCO was incubated overnight (30 °C, 20 h, shaking) in buffer containing 50 mM HEPES (pH 8.0), 2 mM $MgCl_2$, and 0.5 mM GDP with 5 mM azido-proxyl (from a 200 mM stock solution in DMSO, 2.5/100 v/v). Unbound spin labels were removed using Zeba desalting columns (2 ml, 7 kDa cutoff, 2 runs). Finally, the protein solutions were concentrated in Amicon Ultra-4 centrifugal devices (3 kDa cutoff) to reach a final protein concentration of 50 µM. The labelling efficiency was determined to be approximately 10%.

Sample composition for FRET and EPR measurements

In the FRET experiments with lipidated N-Ras, the following sample composition (70 µl volume) was used: 100 nM donor protein, 335 nM acceptor protein, 100 µM POPC (400 nm liposomes), and 2.5 mM DTT in buffer (50 mM Hepes (pH 7.5), 50 mM NaCl, 2 mM $MgCl_2$, and 20 µM GDP. The data were recorded after 3 h incubation at 25 °C. All measurements with lipidated protein and POPC liposomes were reproduced on a second sample and each sample was measured four times. For measurements without POPC liposomes one sample was measured four times. For the measurement of non-lipidated samples, 100 nM donor protein, 240 nM acceptor protein, 100 µM POPC (400 nm liposomes), and 2.5 mM DTT were used. These samples were measured four times as well. Prior to EPR measurements, POPC liposomes were incubated with spin labeled Ras in a protein-lipid ratio of 1:100 for 15 min at RT.

Supporting Note 4: Experimental set up and analysis of FRET measurements

TCSPC measurements and analysis

The fluorophore's lifetimes were measured using a TCSPC setup from PicoQuant (Berlin, Germany). The data were acquired with a pulsed laser-diode, emitting at 510 nm (LDH-D-C-series) driven by a PDL 800-D laser driver, a photomultiplier detector module (PMA 182-N-M) equipped with a holder for proper filters, and a Pico Harp 300 Photon-Counting System. To avoid pile-up effects, the laser intensity was adjusted so the detected photon count rate did not exceed 1% of the excitation rate (10 MHz). Photon events were stored in histograms bins with a width of 4 ps. The recording time for each sample was 40 min and the integration time for each histogram was 600 s, resulting in 4 histograms for each sample. The FRET efficiency was determined by measuring the donor's lifetime with (τ_{DA}) and without (τ_D) the presence of the acceptor. In this way, fluorescence data were obtained for N-Ras S106-Atto 532/Atto 655, N-Ras T124-Atto 532/Atto 655 C118S, and N-Ras E49Q S106-Atto 532/Atto 655 C118S D154N. Data were analyzed using the FluoFit Pro software from PicoQuant (Berlin, Germany). The histograms were iteratively reconvoluted by using the instrument response function (IRF) with equation 1.

$$I(t) = \int_{-\infty}^{t} IRF\,(t') \sum_{i=1}^{n} A_i \cdot e^{\frac{t-t'}{\tau_i}} dt' \qquad (1)$$

Where n is the required number of exponential functions, t is the time (ns), A_i is the amplitude of the respective exponential term, and τ_i is the corresponding lifetime. The data of the measurements were evaluated with 3 functions, except the data of the measurement with the fluorophores coupled to T124 of lipidated N-Ras without POPC where 2 functions were used. The resulting lifetimes were amplitude weighted using equation 2.

$$\tau_{a.w.=}\frac{A_1\cdot\tau_1+A_2\cdot\tau_2+\cdots+A_n\cdot\tau_n}{A_1+A_2+\cdots+A_n} \qquad (2)$$

The FRET efficiency E was calculated using the amplitude-weighted lifetimes according to equation 3.

$$E = 1-\frac{\tau_{DA}}{\tau_D}=\frac{R_0^6}{R_0^6+r^6}\rightarrow r=(\frac{R_0^6\cdot(1-E)}{E})^{\frac{1}{6}} \qquad (3)$$

Determination of the corrected FRET efficiencies

Our sample consists of three types of Ras molecules, with D = donor label, A = acceptor label, and X = unlabeled protein. Unlabeled protein is always present since the labeling efficiencies were not 100%. Thus, the detected lifetime τ_{DA} consists of signals derived from Ras dimers with and without acceptor. Therefore, a corrected FRET efficiency (E_{corr}) must be used. This is the FRET efficiency that would be measured in the case of 100 % dimers with one donor and one acceptor label as assumed in formula 1. E_{corr} is determined as described in the supplementary information.

Calculation of the Försterradius R_0

R_0 is determined to be:

$$R_0 = 0{,}211\cdot(J\kappa^2\Phi_{FD}n^{-4})^{\frac{1}{6}} \qquad (4)$$

For the calculation of R_0 the spectral overlap integral J(λ) ($nm^4\cdot M^{-1}\cdot cm^{-1}$) between the donor's emission and the acceptor's absorbance spectrum is needed and is defined as:

$$J(\lambda)=\frac{\int_{-\infty}^{\infty}F_D(\lambda)\cdot\varepsilon_A(\lambda)\cdot\lambda^4\,d\lambda}{\int_{-\infty}^{\infty}F_D(\lambda)\,d\lambda} \qquad (5)$$

Therefore, the emission spectrum of Atto 532 (donor) and the absorption spectrum of Atto 655 (acceptor) were recorded between 520 and 700 nm. The Lambert-Beer's-Law was used to transfer the acceptor-absorption spectrum to an extinction-coefficient-spectrum. J (λ) was determined to be:

$$J(\lambda)=\frac{\int_{520}^{700}F_D(\lambda)\cdot\varepsilon_A(\lambda)\cdot\lambda^4\,d\lambda}{\int_{520}^{700}F_D(\lambda)\,d\lambda}=\frac{1.8647\cdot10^{19}}{1.1632\cdot10^{4}}$$

$$=1.6031\cdot10^{15}$$

$$[J]=[M^{-1}\cdot cm^{-1}\cdot nm^4] \qquad (6)$$

κ^2 is the dipole orientation factor of the fluorophores and amounts to 2/3 of free rotating fluorophores as we expect in our experiments. The quantum yield Φ is 0.9 for Atto 532 as stated by the manufacturer and n is expected to be 1.4. With this, R_0 is calculated as followed:

$$R_0 = 0.211 \cdot (J\kappa^2 \Phi_{FD} n^{-4})^{\frac{1}{6}} = 53.6 \text{ Å} \quad (7)$$

Using the Förster radius, the FRET-efficiencies were transferred into distances according to equation 4. The averages of the measurements with the related standard deviations were calculated. The standard deviation of the nucleotide-nucleotide distance (46 ± 6 Å) of the previously mentioned measurements [1] was adapted to our error calculation and resulted in 46.3 ± 1.4 Å.

Calculation of the corrected FRET efficiency

In order to calculate the corrected FRET efficiency E_{corr} that is connected to the distance of interest, we have to consider our sample composition. An example is given in Table S12. Dimers are randomly formed between donor labeled Ras (D), acceptor labeled Ras (A) and unlabeled Ras (X) in the sample. The probability of each dimer composition is calculated in the column "Probability" of Table S12 based on the fractions of each form. Only the fluorescence of the DA and AD dimers can be influenced by FRET. The dimers without a donor label will not give rise to any fluorescence signal. The dimers XD, DX and DD (weighted twice) will give rise to a fluorescence signal that is not influenced by FRET, because of the lack of an acceptor. The measured experimental fluorescence lifetime τ_{exp} is therefore a weighted average value of the lifetimes without (τ_D) and with (τ_{DA}) acceptor, each multiplied with the respective fraction:

$$\tau_{exp} = \text{fraction without acceptor} \cdot \tau_D + \text{fraction with acceptor} \cdot \tau_{DA} \quad (8)$$

For the calculation, the ratio of donor labeled protein in complex with an acceptor with all donor labeled proteins has to be used. As an example for a sample with D = 100 nM, A = 335 nM, X = 403 nM is shown below. Here, 40 % (0.096 out of 0.238) of the donor labelled protein is in a dimer with an acceptor labelled protein. This means for the lifetime τ_{DA}:

$$\tau_{DA\,exp} = 0.6 \cdot \tau_D + 0.4 \cdot \tau_{DA}$$

$$\tau_{DA} = 2.5 \cdot \tau_{DA\,exp} - 1.5 \cdot \tau_D \quad (9)$$

The corrected FRET efficiency E_{corr} that is used for the distance calculation is calculated as follows:

$$E_{corr} = 1 - \frac{2.5 \cdot \tau_{DA\,exp} - 1.5 \cdot \tau_D}{\tau_D} = \left(1 - \frac{\tau_{DA\,exp}}{\tau_D}\right) \cdot 2.5 \quad (10)$$

We calculate the fluorophore distances based on the determined FRET efficiencies according to

$$E = \frac{1}{1 + \left(\frac{r}{R_0}\right)^6} \quad (4)$$

where E is the FRET efficiency, r is the distance between the donor and acceptor fluorophore. The Förster radius R_0 = 53.6 Å was calculated as described in materials and methods. The calculation leads to r = 43.3 ± 2.3 Å for lipidated N-Ras on POPC liposomes with fluorophores at position 106 and to r = 72 ± 3.5 Å for lipidated N-Ras on POPC liposomes with fluorophores at position 124. The distance between the nucleotides (46.3 ± 1.4 Å) was obtained from the literature [9] and subjected to the error calculation used in this manuscript.

Supporting Note 5: Calculation of distance distributions using the PyMOL MtsslWizard

The dimer conformations (Table S3) were evaluated based on the agreement with FRET and EPR experiments. The distance distributions for the three FRET pairs S106-Atto532/S106-Atto655, T124-Atto532/T124-Atto655, MANT-Ribose/TNP-Ribose and for the EPR label pair T124-Proxyl/T124-Proxyl of a representative structure of each the 64 identified conformation and their subcategories were calculated using the PyMOL plugin MtsslWizard [21]. The fluorophores Atto 532, Atto 655, Mant-GDP, and TNP-GDP were integrated in the software by following manufacturer's instructions. The EPR label proxyl was already available in the software. The "vdW restraints" setting was set to "loose" and the parameters have been set to try to find 200 rotamers. First, the fluorophore Atto532 was superimposed to the backbone of residues S106 of monomer A and Atto655 to S106 of monomer B. Then, the mtsslWizard plugin generated conformational ensembles and calculated the corresponding distance distributions between the fluorophores as shown exemplarily in Fig. S5. A gaussian fit of the distance distribution gives the mean values and standard deviations of the FRET distance. The same protocol was carried out for T124A/T124B and for T124A-Proxyl/T124B-Proxyl. For the nucleotides, the FRET-pair Mant-/TNP-Ribose was superimposed on the ribose group of the nucleotide. In Table S3 all mean distances and standard deviations are summarized, compared, and evaluated with respect to the agreement with the experimental values.

Supporting Note 6: Biomolecular simulations

Workflow and run parameters

In the following the general workflow and the parameters used for all biomolecular simulations performed in this publication with exception of the SCO-proxyl simulations are described. Dimer structures were prepared for simulation using the MOBY/MAXIMOBY program package (CHEOPS Molecular Modeling, Altenberge, Germany). The protein was protonated based on pK(a) calculation. Experimentally resolved protein internal water molecules were deleted and then water molecules of the first solvation shell were added using the Vedani algorithm, which is based on the directionality of hydrogen bonds. Energetically unfavorable side chain and back bone conformations were visualized and interactively optimized with MOBY. Next, the dimer structure was placed with the anchors attached to a POPC bilayer analog as previously described [1]. A cubic simulation box with periodic boundary conditions filled with TIP4P water and a physiological salt concentration of 154 mmol/l, using sodium cations and chlorine anions was generated. The ion ratio was adjusted to ensure the neutral charge of the simulation system.

Classical molecular mechanic simulations were performed with GROMACS 2019[22] using the optimized-potentials-for-liquid-simulations all-atom (OPLS-AA) force field. The parameters for GTP and GDP were the same as the ones presented by Rudack et al.[23] The parameters for the

palmitoyl and farnesyl anchor of Ras were the same as the ones used by Güldenhaupt et al.[1] For the POPC bilayer previously reported parameters from Ulmschneider et al.[24] were used.
Electronic interactions were determined by the Fast Particle-Mesh Ewald method using a grid spacing of 0.12 nm, fourth order spine interpolation and a cut-off value of 1.0 nm. For van der Waals interactions, a cut-off value of 1.0 nm was employed. All bonds were constrained to their equilibrium length using the LINCS algorithm.
First, the system energy was minimized using the steepest descent algorithm, constraining the protein and the Vedani water molecules to minimize the bulk water molecules and the membrane lipids. Subsequently, a conjugated gradient minimization was performed while constraining only the protein backbone, to allow for further optimization of the side chains and the Vedani water molecules. The system was heated up over a course of 1.6 ns with a linear gradient from 150 K to 310 K while restraining the protein. Next, an NVT equilibration run (number of atoms n, the volume V, and the temperature T are constant and the pressure is free) with restrained protein atoms was performed followed by an NPT equilibration run (number of atoms n, the pressure p, and the temperature T are constant and the volume is free) with the protein backbone restrained. Pressure and temperature were kept at constant values of 1 standard atmosphere and 310 K, respectively, using a Berendsen barostat with a coupling constant of 1.0 ps and a modified Berendsen thermostat (V-rescale) with a coupling constant of 0.1 ps. The final production run was carried out using time intervals of 2 fs.

Input structure preparation
We aligned the initial N-Ras-GDP monomer to all selected conformations to transform them all to N-Ras-GDP dimers for further computational refinement. We picked N-Ras-GDP as we performed all experiments in this publication with N-Ras-GDP. Next, we connected the HVR and the anchor to the dimers to attach them to a POPC membrane. Therefore, the region from residue 173 to 186, which is not resolved in any x-ray structures due to its flexibility, was taken from an equilibrated simulation structure from Güldenhaupt et al.[1] and connected to the above obtained G-domains of the dimer structure. Finally, all systems are simulated following the workflow and parameters given in biomolecular simulations sections of material and methods.

Analysis
The simulations were analyzed as follows. The RMSD calculation was performed with Gromacs 2019 for the Cα atoms of the residue 1-172 with a time step of 5 ps. Contact analysis was done within the MOBY/MAXIMOBY program package. Every simulation was divided in 1000 frames and analyzed regarding hydrogen bonds/salt bridges and van der Waals contacts. The analysis of hydrogen bonds/salt bridges is based on distance as well as geometrical conditions. The resulting contact matrix displays a binary result for every frame (contact or no contact). For every ten frames, a representative frame was written so that the final contact matrix contained 100 frames. The intermolecular contacts between the monomers are shown in Fig. S7.
The calculation of the representative structure started with the same 1000 frame contact matrix with two additional components: A secondary structure analysis for every residue based on the psi and phi angles and an assignment of side chain chi angles in categories of 60° increments. The frame with the least difference to all other frames was taken as the representative structure.
For every representative structure the distance distribution for the three FRET pairs S106-Atto532/S106-Atto655, T124-Atto532/T124-Atto655, MANT-Ribose/TNP-Ribose and for the EPR label pair T124-Proxyl/T124-Proxyl was calculated as described in supporting note 6.

Conformation I.5 displays an equilibrated RMSD after 400 ns and shows a stable one-sided salt bridge between D154/R161 (Fig. S7). This contact is also present and stable in all other

simulations except I.1 and I.6. Simulations I.7 and I.8 exhibit a two-sided D154/R161 contact. Several other intermolecular contacts are observed (Fig. S7). Analysis of these shows a stabilizing effect of the E49-H131 contact, while others fluctuate between simulations and do not show a consistent pattern (Table S6).
The overall unstable binding pattern of I.6 correlates with its RMSD, which does not equilibrate in the given time. I.7 displays a stable RMSD after approximately 500 ns, while I.8 is stable after 250 ns (Fig. S7). The simulations I.9 and I.10 equilibrate within the first 50 ns (Fig. S7) and their representative structures fulfill the experimental criteria for the FRET and EPR distance distributions (Table S7). Conformation I.11 does not equilibrate in the given simulation time, while I.12 stabilizes after 300 ns (Fig. S7).

Supporting Note 7: Experimental set up and analysis of EPR measurements

EPR spectroscopy
DEER (also known as PELDOR) experiments were performed at Q-band frequencies (34 GHz) with a Bruker Elexsys 580 spectrometer equipped with a Q-band bridge and a 150 W Q-band travelling wave tube (TWT) amplifier (Applied Systems Engineering, Fort Worth, TX, USA), using a Bruker Flexline resonator ER 5106QT-2. The 3 mm outer diameter EPR quartz capillaries were loaded with 50 µl of proteoliposome suspension containing 25% glycerol. The temperature was stabilized at 50 K using a continuous flow helium cryostat CF935 (Oxford Instruments, Abingdon, UK) regulated by temperature controller ITC 503S (Oxford Instruments). All measurements were performed using the four-pulse DEER sequence[25, 26]:

$\pi/2\ (\nu_{obs})$ - τ_1 - $\pi\ (\nu_{obs})$ - t' - $\pi\ (\nu_{pump})$ - $(\tau_1 + \tau_2 - t')$ - $\pi\ (\nu_{obs})$ - τ_2 - echo

A two-step phase cycling, (+)x and (-)x, was performed on $\pi/2$ (ν_{obs}). Time t' was varied, while τ_1 and τ_2 were kept constant. The dipolar evolution time was given by $t = t' - \tau_1$. Data were analyzed only for $t > 0$. The resonator Q was set to approximately 1500 (as determined by the spectrometer software). The pump frequency ν_{pump} was set 30 MHz higher than the resonator dip center, coinciding with the maximum of the EPR spectrum. The observer frequency ν_{obs} was 20 MHz lower than the dip center, yielding a total frequency offset of -50 MHz. The observer pulse lengths were 16 ns for $\pi/2$ and 32 ns for π pulses and the pump pulse length was 16 ns. Proton modulation was averaged by adding traces at 8 different τ_1 values, starting at $\tau_{1,0}$ = 536 ns and incrementally adding 8 ns ($\Delta\tau_1$ = 8 ns). Data points were collected in 8-ns time intervals. The total measurement time was approximately 72 h. Data analysis was performed with the software package DeerAnalysis[27], using a model-based fit assuming a single Gaussian distribution of distances.

Biomolecular simulations to analyze the conformational space sampled by SCO-Proxyl
Biomolecular simulations were used to analyze the conformational space sampled by the SCO-Proxyl spin label side chain at positions 124 of the dimer models. The simulations were carried out in YASARA structure, utilizing the Amber03 force field[28] and Particle Mesh Ewald summation for long range electrostatic interactions with a cutoff at 8 Å. The time step for the calculation of intramolecular forces was 0.5 fs (simulation sub-step). The intermolecular forces have been calculated every 2 simulation sub-steps. The simulation temperature was 298.0 K. Temperature control was carried out by rescaling atom velocities. Pressure control was achieved by keeping the solvent (H_2O) density at 0.997 g/ml and rescaling the simulation cell along all three axes.

During the 30 ns long simulations the protein backbone was kept fixed. Simulation snapshots were acquired in steps of 25 ps and analyzed in terms of inter spin distances (nitroxide-nitroxide). For preparation of the ‘rotamer clouds’ spin label side chain structures were acquired in steps of 250 ps.

Supplementary Figures

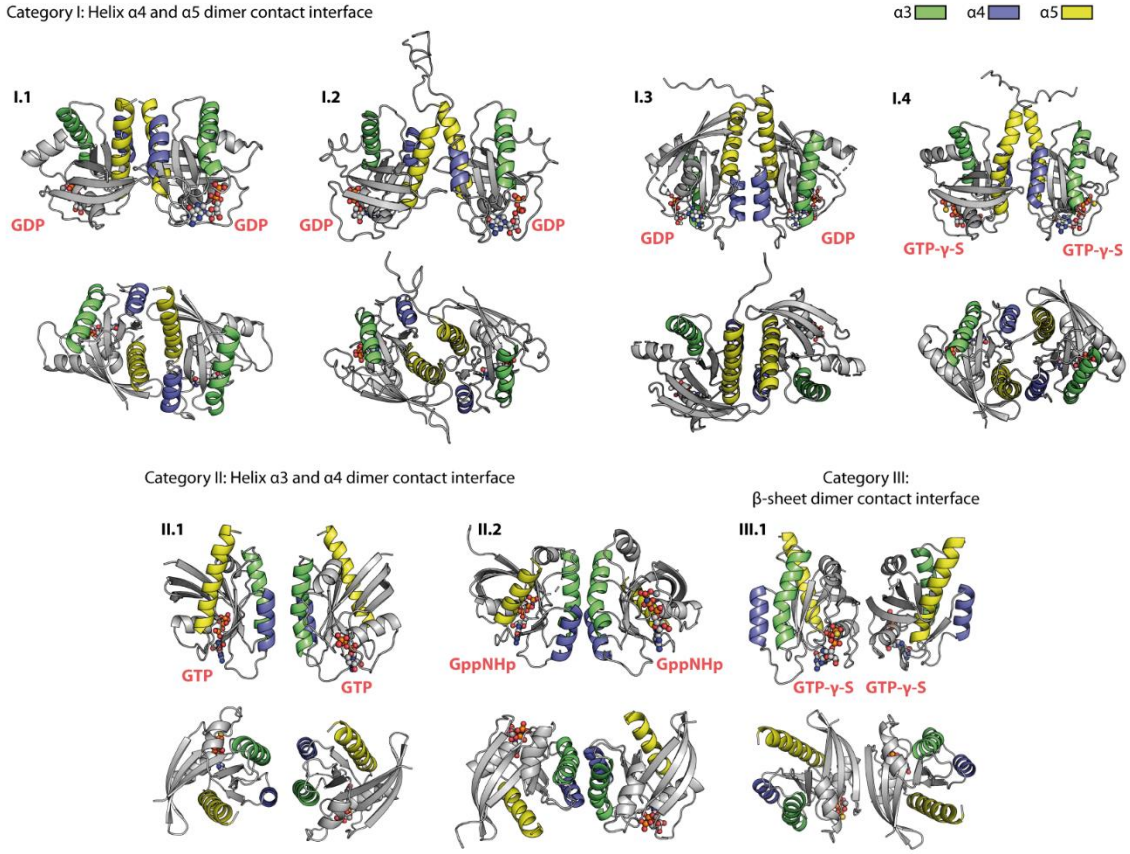

Fig. S1. Diversity of previously proposed different Ras dimer structural models. To order the huge variety of the published dimer structural models we divided them into three substantially different main categories based on the relative orientation of the monomers. These categories are further subdivided based on the detailed dimer interaction interface. The key helices are represented by different colors (helix α3: green, helix α 4: blue, helix α5: yellow) and the nucleotides are displayed in spherical shape. The category I dimer interface is formed by contacts of helices α 4 and α 5. Model I.1 is the most common interface found in the crystal packing of Ras X-ray structures of all isoforms.[1] Model I.2 is the full-length membrane attached N-Ras-GDP dimer structure resulting after refinement of model I.1 through biomolecular simulations.[1] Model I.2 is very similar to a model for K-Ras-GTP obtained by protein docking combined with biomolecular simulations.[4] Model I.3 (protein data bank ID 6W4F) was obtained using the high ambiguity driven protein−protein docking (HADDOCK) protein docking software with distance restraints from NMR.[2] Using the same methods, the authors also published a K-Ras4B-GTP-ɣ-S structure (PDB-ID: 6W4E) referred to as model I.4. The category II dimer interface is formed by contacts of helices α3 and α4. Model II.1 is a structure obtained through simulations performed by Prakash et al[4]. Model II.2 is the "α-Homodimer" obtained from the PRISM protein-protein docking server[6] by Muratcioglu et al[3]. Model III.1 is the "β-Homodimer"[3] also obtained in the same study through PRISM.

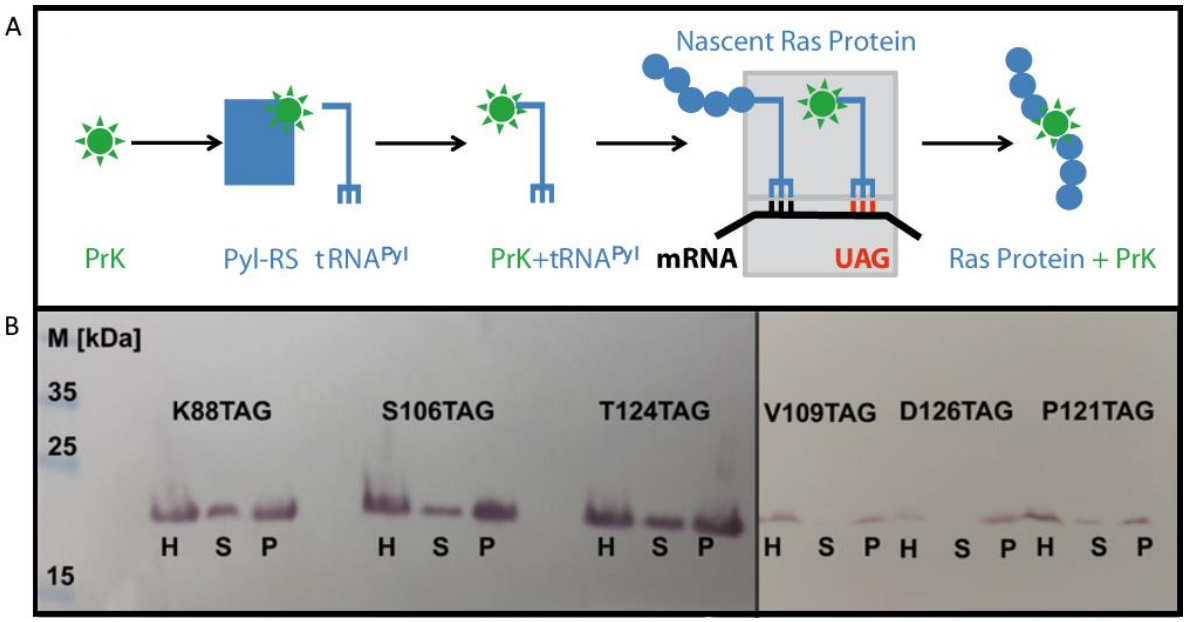

Fig. S2: Experimental strategy to incorporate unnatural amino acids into Ras. For site specificity of the second modification, we developed the strategy shown in **A** to incorporate a biorthogonal alkyne moiety as part of the unnatural amino acids (uaa) N-propargyl-L-lysine (PrK) and Cyclooctyne-Lysine (ScO) into N-Ras. **B** shows Western Blot results that were obtained after the incorporation of the unnatural amino acid at different sites of N-Ras. A clear band in the supernatant represents a good possibility to obtain N-Ras with unnatural amino acid at respective site. Only the mutants K88TAG, S106TAG and T124TAG show a clear band in the supernatant. H = Homogenate, S = Supernatant, P = Pellet. The position T124 was chosen for the attachment of the fluorophore, as it displayed the highest yield. Due to the proximity of K88 to T124 we chose S106 as the second label site, resulting in a better distribution of the fluorophores across the protein.

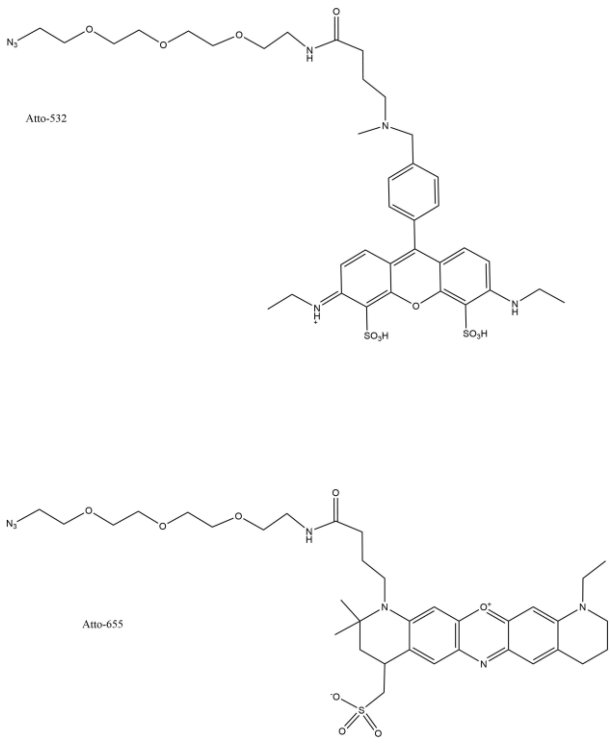

Fig. S3: Chemical drawings of the FRET labels Atto-532 and Atto-655 used for FRET experiments.

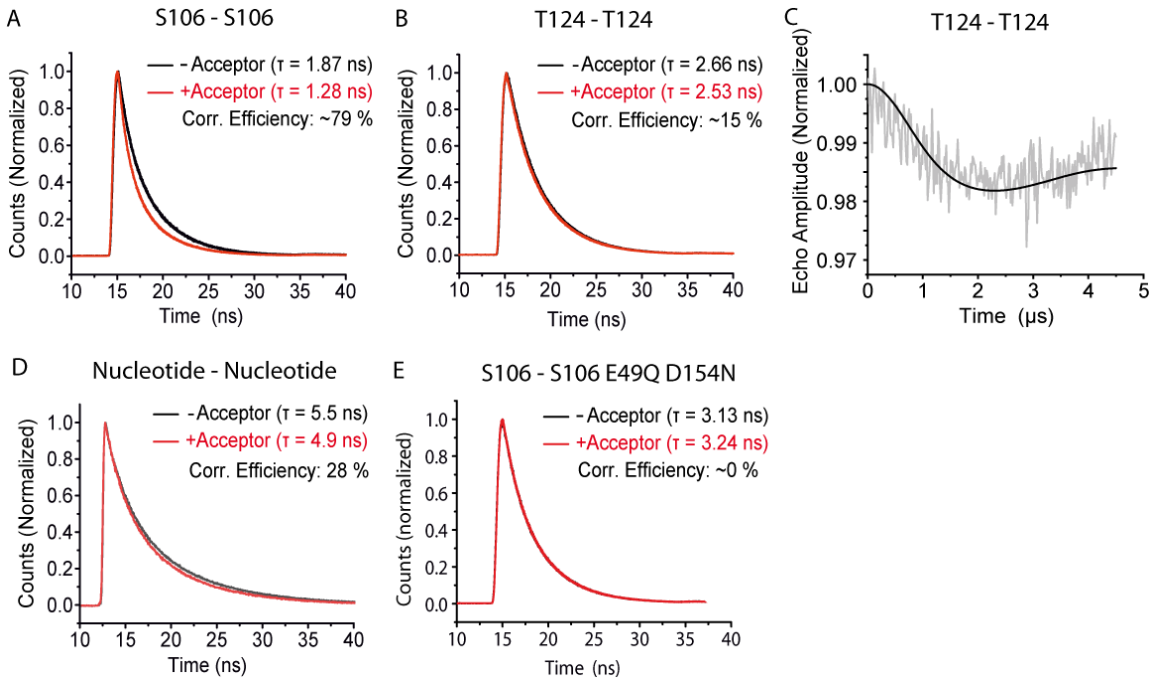

Fig. S4: Experimental FRET and EPR measurements. The time-correlated single photon counting (TCSPC) histograms of membrane-bound N-Ras-GDP S106-Atto532 (**A**) and T124-Atto532 C118S (**B**) with (red) and without (black) the acceptors N-Ras-GDP S106-Atto655 or T124-Atto655 C118S are shown. **C** shows the normalized experimental EPR (DEER) data for membrane-bound N-Ras-GDP T124-Proxyl. **D** displays the TCSPC histogram of membrane-bound N-Ras with the fluorescent nucleotide MANT-GDP in presence (red) and in absence of the acceptor N-Ras (TNP-GDP; black), which was published previously by Güldenhaupt et al.[1] **E** shows the TCSPC histogram of membrane bound N-Ras-GDP S106-Atto532 with (red) and without (black) the acceptors N-Ras-GDP S106-Atto655 of the E49Q D154N double mutant. The presence of the acceptor leads to a decrease in the lifetimes of the donors due to FRET. Histograms were normalized.

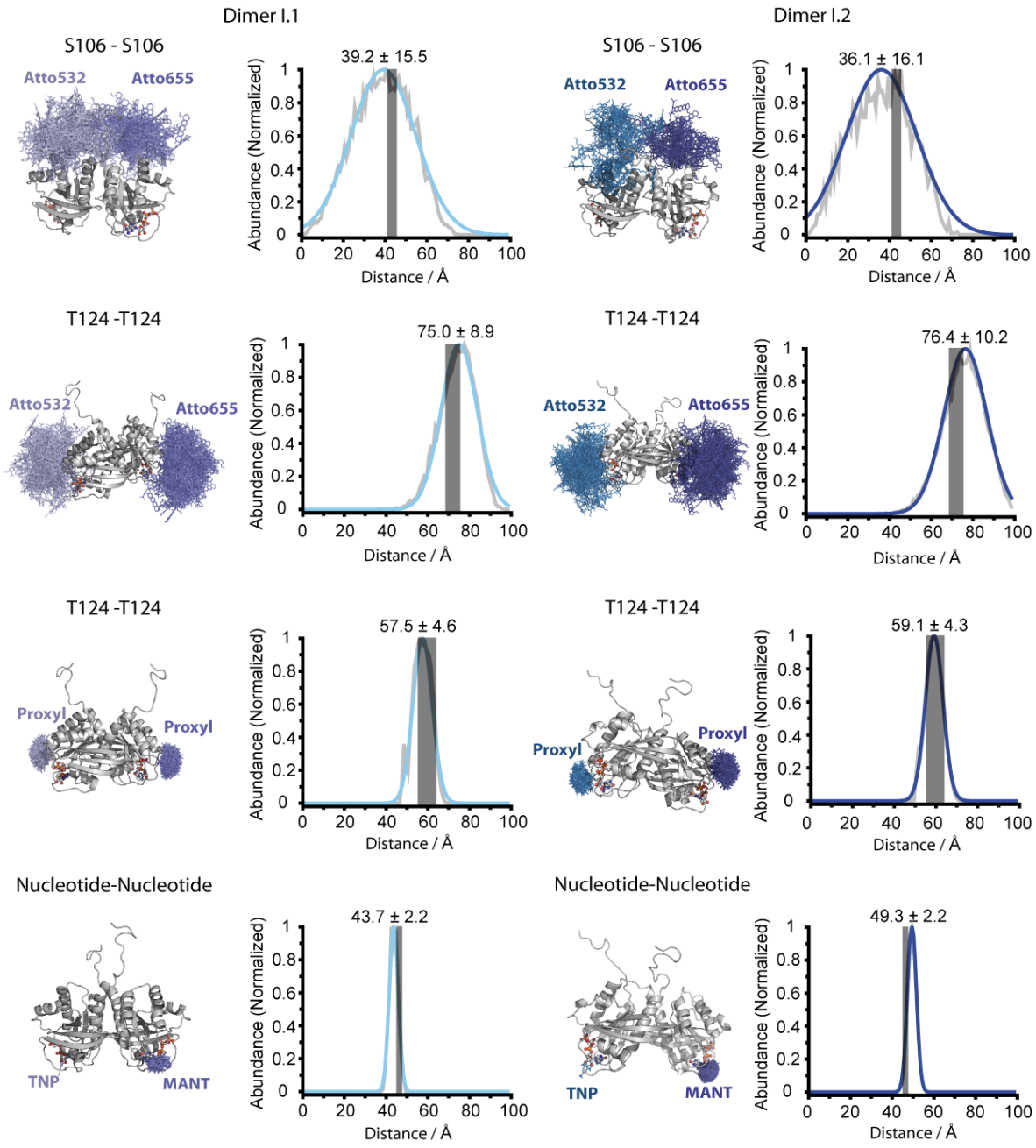
Dimer I.1
Dimer I.2
S106 - S106
Atto532
Atto655
39.2 ± 15.5
36.1 ± 16.1
T124 -T124
75.0 ± 8.9
76.4 ± 10.2
Proxyl
57.5 ± 4.6
59.1 ± 4.3
Nucleotide-Nucleotide
TNP
MANT
43.7 ± 2.2
49.3 ± 2.2
Abundance (Normalized)
Distance / Å

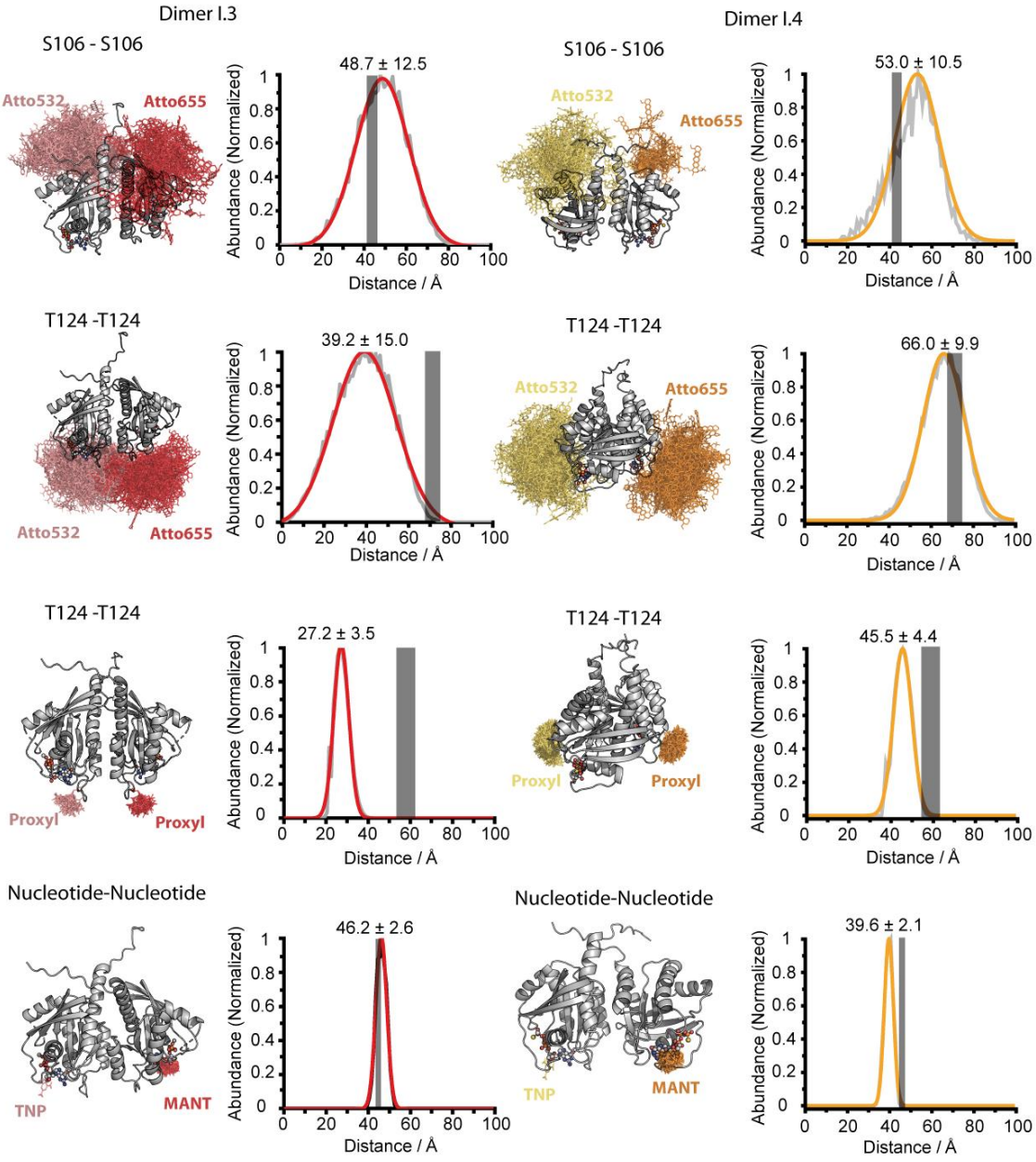
Dimer I.3
S106 - S106
Atto532
Atto655
48.7 ± 12.5
Abundance (Normalized)
Distance / Å
Dimer I.4
S106 - S106
Atto532
Atto655
53.0 ± 10.5
Abundance (Normalized)
Distance / Å
T124 -T124
Atto532
Atto655
39.2 ± 15.0
Abundance (Normalized)
Distance / Å
T124 -T124
Atto532
Atto655
66.0 ± 9.9
Abundance (Normalized)
Distance / Å
T124 -T124
Proxyl
Proxyl
27.2 ± 3.5
Abundance (Normalized)
Distance / Å
T124 -T124
Proxyl
Proxyl
45.5 ± 4.4
Abundance (Normalized)
Distance / Å
Nucleotide-Nucleotide
TNP
MANT
46.2 ± 2.6
Abundance (Normalized)
Distance / Å
Nucleotide-Nucleotide
TNP
MANT
39.6 ± 2.1
Abundance (Normalized)
Distance / Å

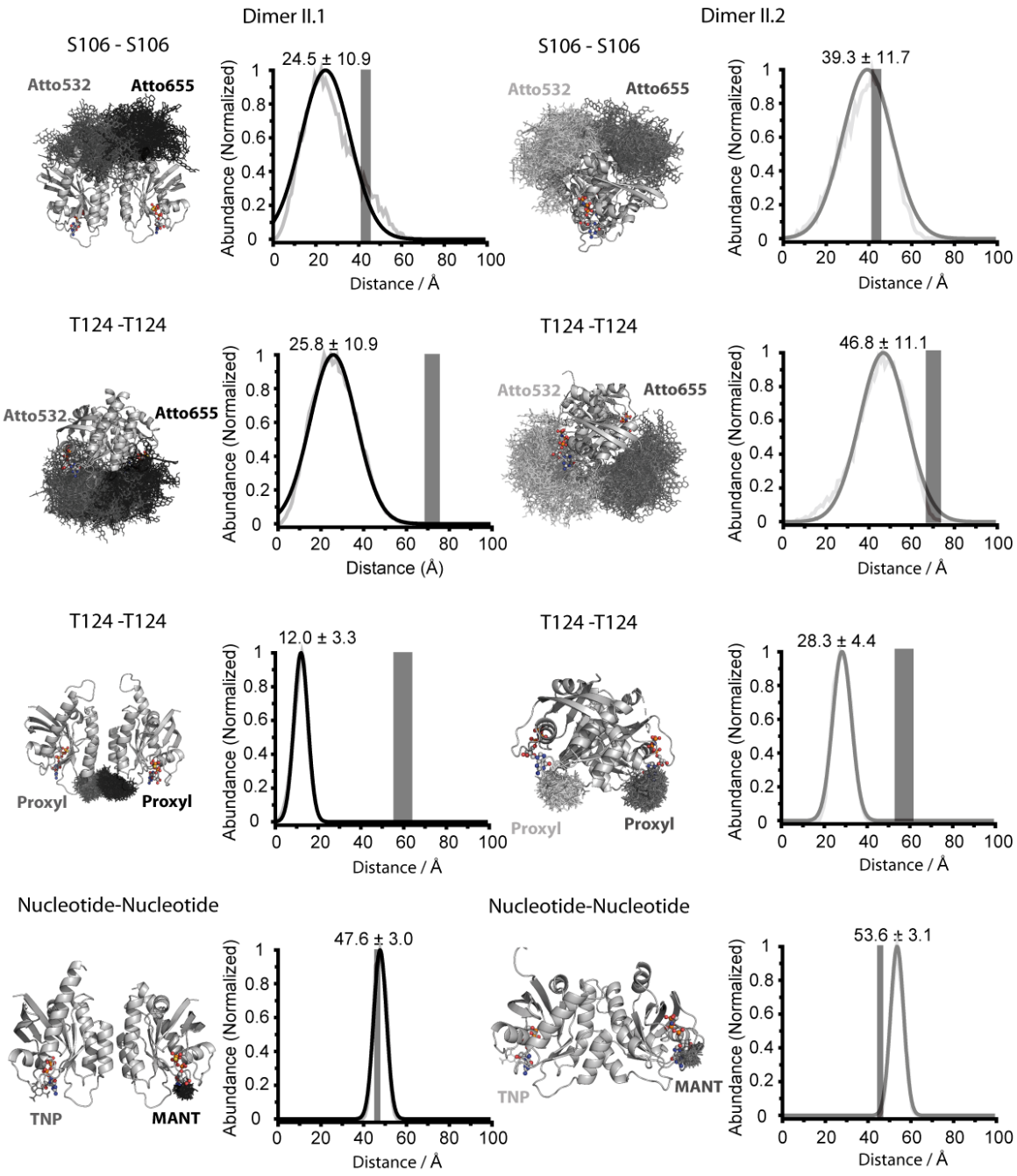
Dimer II.1
Dimer II.2
S106 - S106
Atto532
Atto655
24.5 ± 10.9
39.3 ± 11.7
T124 -T124
25.8 ± 10.9
46.8 ± 11.1
Proxyl
12.0 ± 3.3
28.3 ± 4.4
Nucleotide-Nucleotide
TNP
MANT
47.6 ± 3.0
53.6 ± 3.1
Abundance (Normalized)
Distance / Å
Distance (Å)

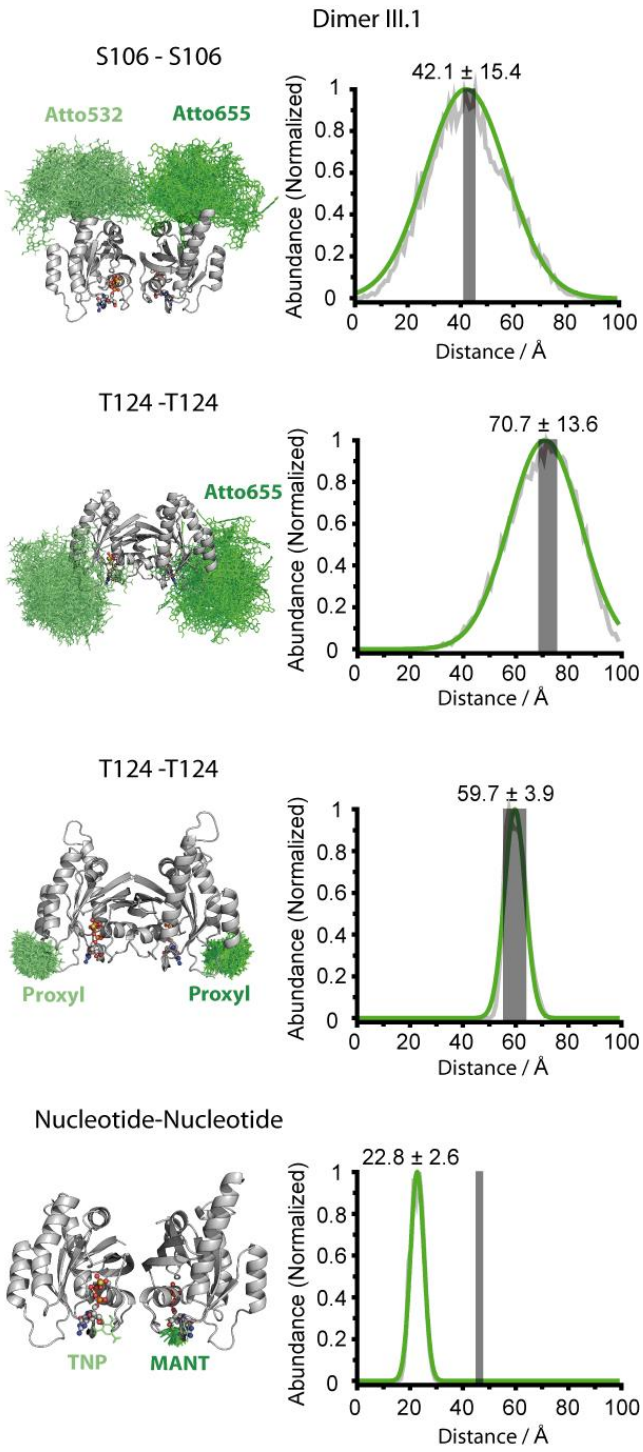

Fig. S5: Calculated distance distributions between protein-bound fluorophores of published possible dimer structural models. The FRET-pair Atto532/Atto655 was superimposed on the backbone of residues S106 and T124, the FRET-pair Mant-/TNP-Ribose on the ribose group of the nucleotide GDP. The EPR spin label proxyl was superimposed on the backbone of T124. The tool mtsslWizard[21] generated conformational ensembles and calculated the corresponding distance distributions between them for S106-S106, T124-T124 and nucleotide-nucleotide. A gaussian fit of the data gives the mean values of the distributions.

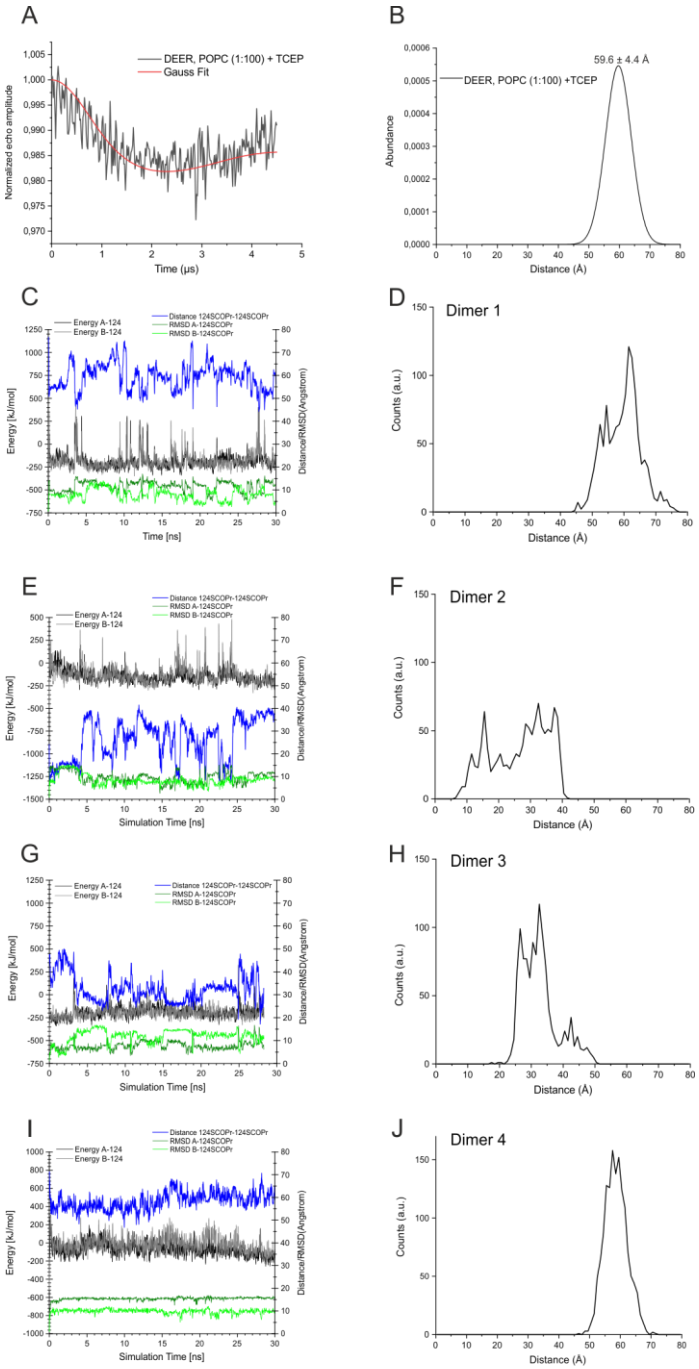

Fig. S6: Experimental EPR data and theoretical distance distributions obtained by MD simulations. A shows the experimental DEER data that were described by a Gauss Fit (red line). **B** displays the resulting distance distribution with a main peak at 59.7 ± 2.5 Å. **C**, **E**, **G** and **I** show the analysis of the MD simulations, that were performed in order to get theoretical distance distributions between two EPR spin labels (Proxyl) attached to one of the four dimer structure models at position 124. **D**, **F**, **H** and **J** display the theoretical distance distributions that were obtained by MD simulations. Only dimer structure models 1 and 4 are in line with the experimental EPR result.

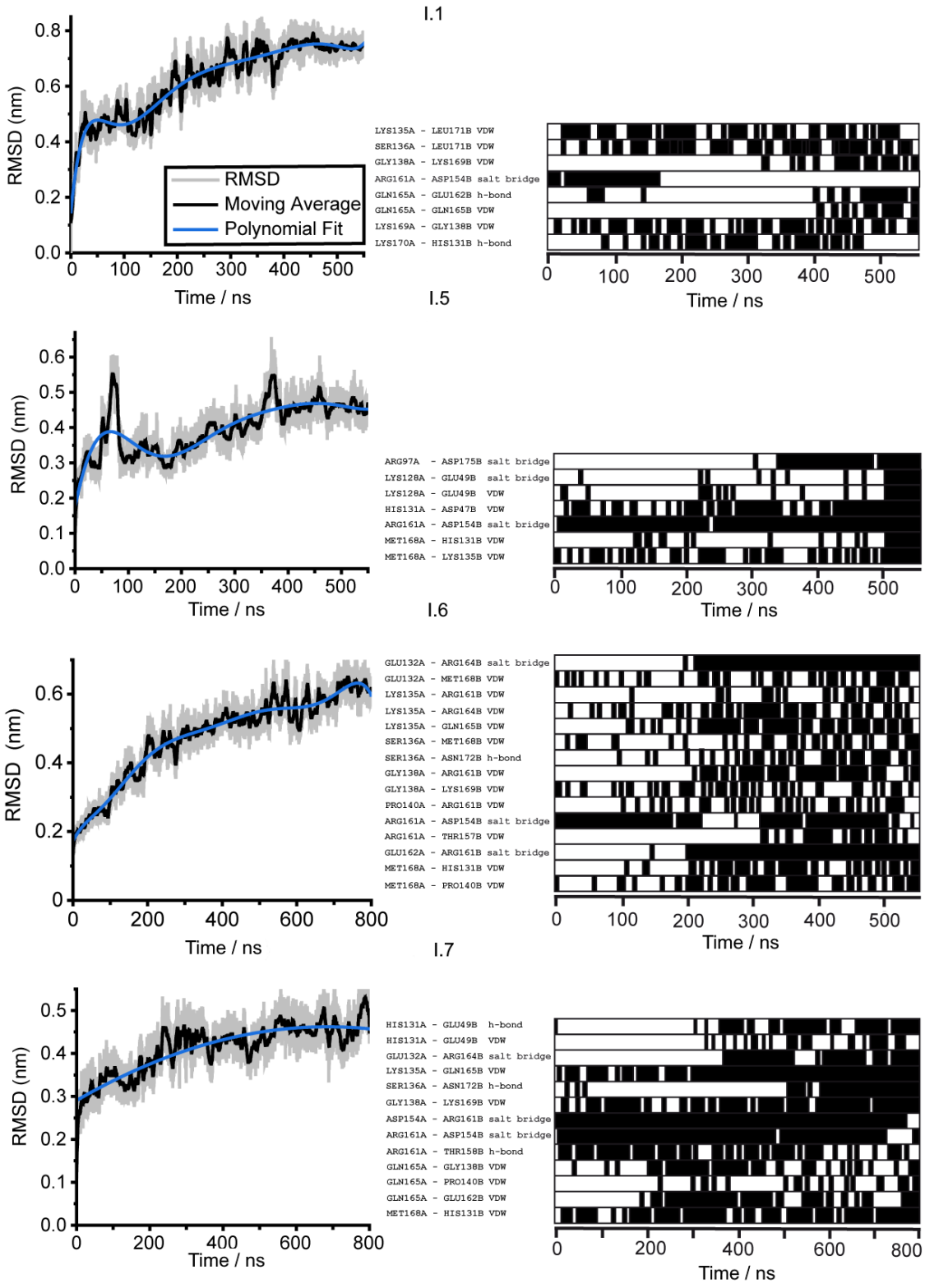
I.1
RMSD (nm)
Time / ns
RMSD
Moving Average
Polynomial Fit
LYS135A - LEU171B VDW
SER136A - LEU171B VDW
GLY138A - LYS169B VDW
ARG161A - ASP154B salt bridge
GLN165A - GLU162B h-bond
GLN165A - GLN165B VDW
LYS169A - GLY138B VDW
LYS170A - HIS131B h-bond
I.5
ARG97A - ASP175B salt bridge
LYS128A - GLU49B salt bridge
LYS128A - GLU49B VDW
HIS131A - ASP47B VDW
ARG161A - ASP154B salt bridge
MET168A - HIS131B VDW
MET168A - LYS135B VDW
I.6
GLU132A - ARG164B salt bridge
GLU132A - MET168B VDW
LYS135A - ARG161B VDW
LYS135A - ARG164B VDW
LYS135A - GLN165B VDW
SER136A - MET168B VDW
SER136A - ASN172B h-bond
GLY138A - ARG161B VDW
GLY138A - LYS169B VDW
PRO140A - ARG161B VDW
ARG161A - ASP154B salt bridge
ARG161A - THR157B VDW
GLU162A - ARG161B salt bridge
MET168A - HIS131B VDW
MET168A - PRO140B VDW
I.7
HIS131A - GLU49B h-bond
HIS131A - GLU49B VDW
GLU132A - ARG164B salt bridge
LYS135A - GLN165B VDW
SER136A - ASN172B h-bond
GLY138A - LYS169B VDW
ASP154A - ARG161B salt bridge
ARG161A - ASP154B salt bridge
ARG161A - THR158B h-bond
GLN165A - GLY138B VDW
GLN165A - PRO140B VDW
GLN165A - GLU162B VDW
MET168A - HIS131B VDW

I.8

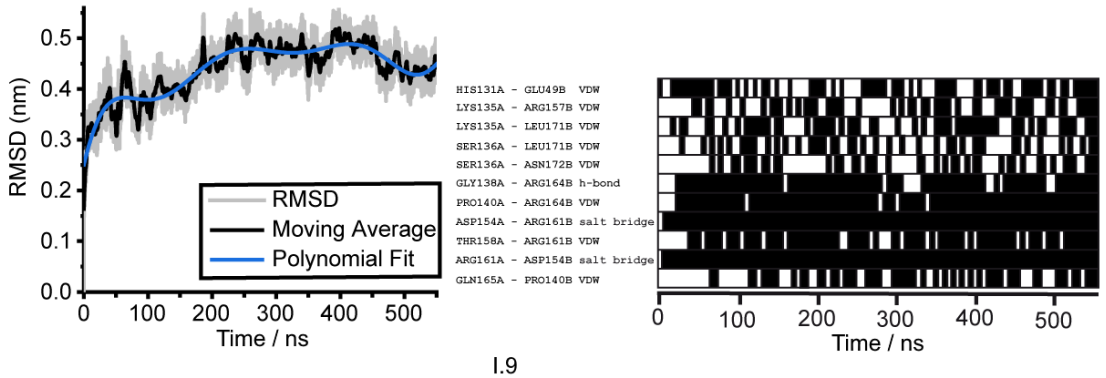
RMSD (nm)
Time / ns
RMSD
Moving Average
Polynomial Fit
HIS131A - GLU49B VDW
LYS135A - ARG157B VDW
LYS135A - LEU171B VDW
SER136A - LEU171B VDW
SER136A - ASN172B VDW
GLY138A - ARG164B h-bond
PRO140A - ARG164B VDW
ASP154A - ARG161B salt bridge
THR158A - ARG161B VDW
ARG161A - ASP154B salt bridge
GLN165A - PRO140B VDW

I.9

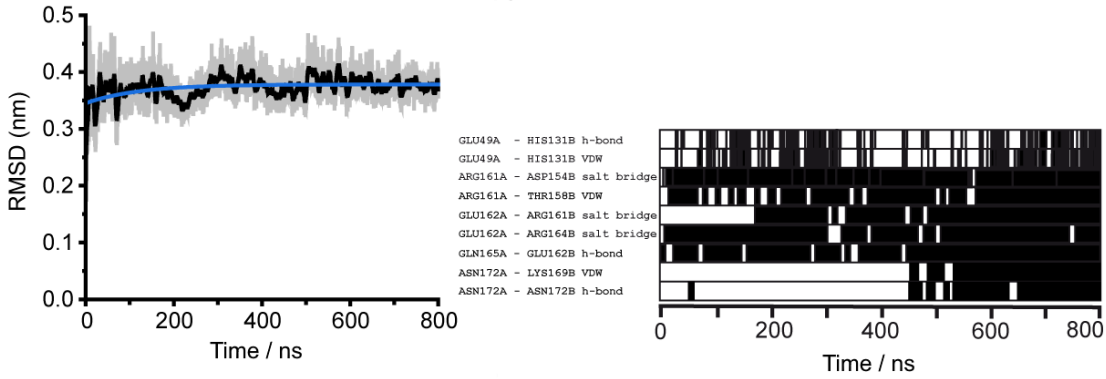
RMSD (nm)
Time / ns
GLU49A - HIS131B h-bond
GLU49A - HIS131B VDW
ARG161A - ASP154B salt bridge
ARG161A - THR158B VDW
GLU162A - ARG161B salt bridge
GLU162A - ARG164B salt bridge
GLN165A - GLU162B h-bond
ASN172A - LYS169B VDW
ASN172A - ASN172B h-bond

I.10

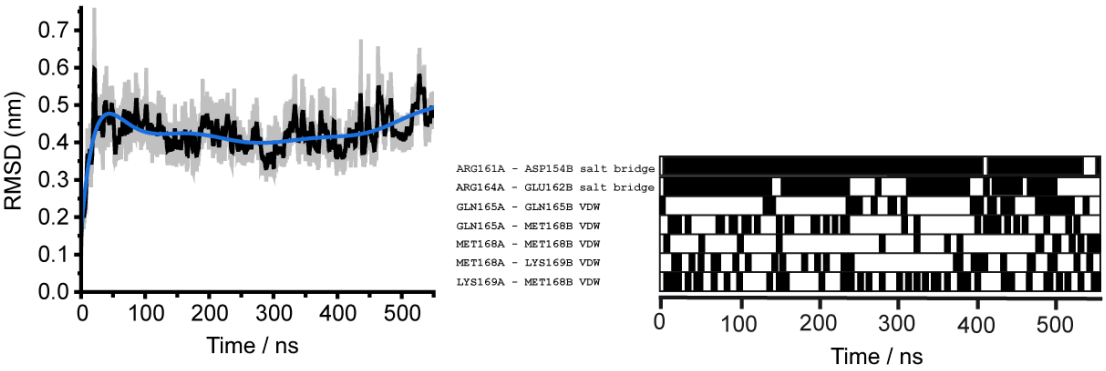
RMSD (nm)
Time / ns
ARG161A - ASP154B salt bridge
ARG164A - GLU162B salt bridge
GLN165A - GLN165B VDW
GLN165A - MET168B VDW
MET168A - MET168B VDW
MET168A - LYS169B VDW
LYS169A - MET168B VDW

I.11

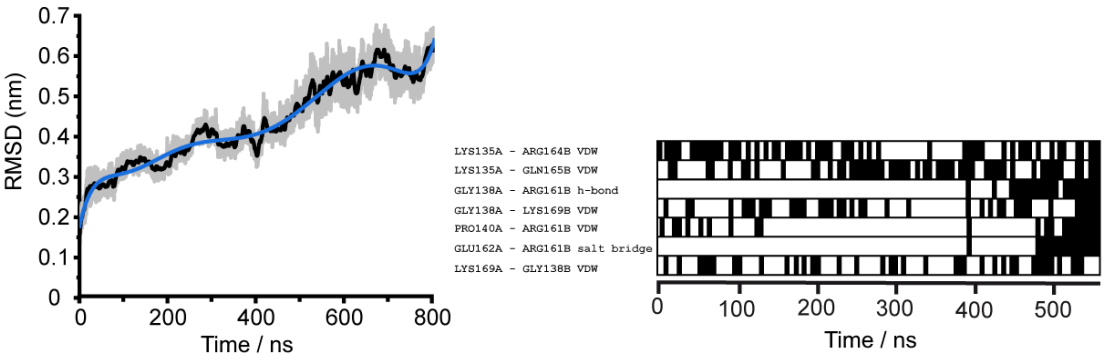
RMSD (nm)
Time / ns
LYS135A - ARG164B VDW
LYS135A - GLN165B VDW
GLY138A - ARG161B h-bond
GLY138A - LYS169B VDW
PRO140A - ARG161B VDW
GLU162A - ARG161B salt bridge
LYS169A - GLY138B VDW

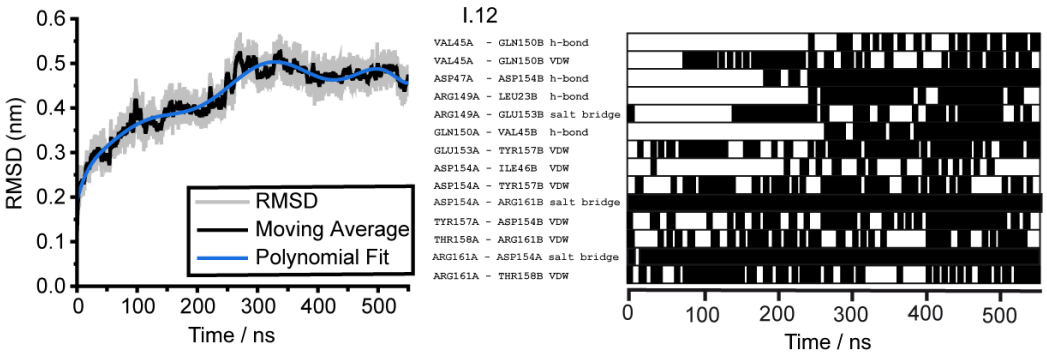

Fig. S7: RMSD and intermolecular contact interface for the Ras dimer simulations (see Table S3-S5). On the left, the RMSD of the Cα atoms for the Ras residues 1-172 is shown (gray). A moving average (black) displays the short-term and a polynomial fit (blue) the long-term trend of the RMSD. Shown on the right, is the dynamic contact interface between the two Ras monomers. A black bar represents an existing contact.

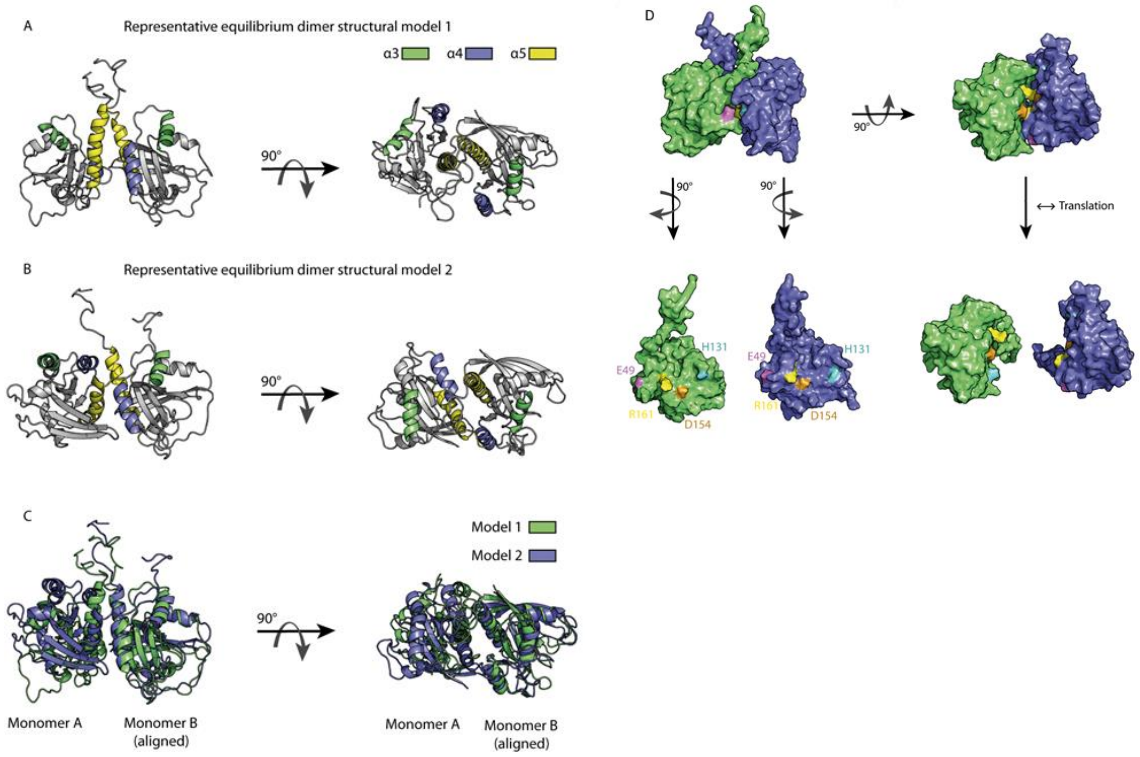

Fig. S8: Representative equilibrium dimer structural models of the lipidated N-Ras dimer simulations. A shows the representative structural model 1 of simulations I.9 and I.10 (see Table S3, S7 and S8), which is in accordance with all experimental values. **B** displays the representative structural model 2 of the other seven simulations (see Table S3, S7 and S8). The helices α3- α5 in **A** and **B** are color coded: Helix α3 (green), helix α4 (blue), helix α5 (yellow). In **C** Monomer B of the representative structural models is aligned to clarify their differences. Model 1 is shown in green, while model 2 is shown in blue. Shown in **D** is the surface of the representative dimer structural model 1. The identified central key interface amino acids R161 (yellow), D154 (orange), E49 (purple) and H131 (cyan) are highlighted. The top left shows the side view of the Ras dimer and the top right the bottom view (rotated by 90 degrees). In the lower left the dimer is folded apart to show the central positions of the key contacts. The bottom right illustrates that the contact surface of the dimer is flat.

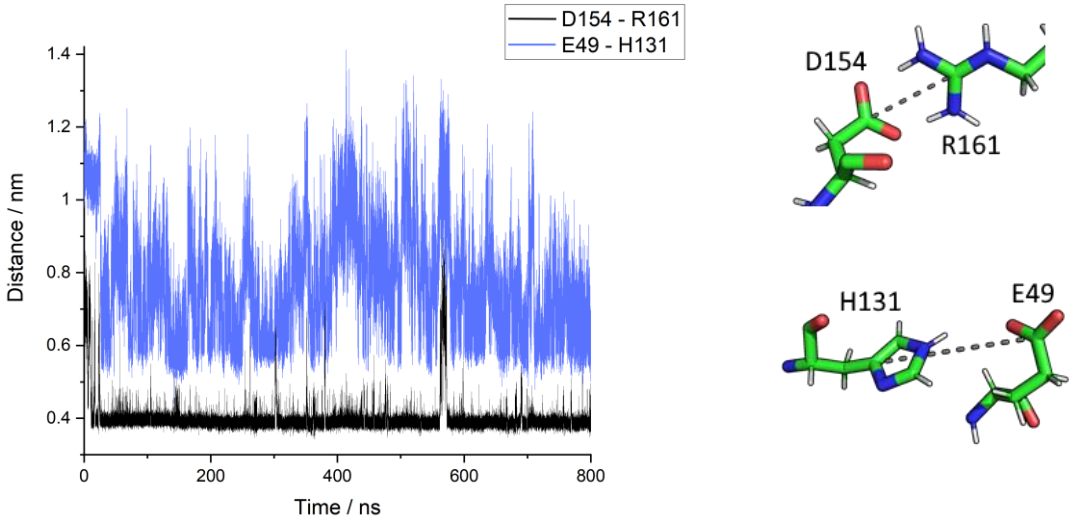

Fig. S9: Distance plot for the most important contact residues of simulation I.9. The distances were measured between CG and CZ for D154-R161, as well as CD and CG for E49-H131 to calculate the distance independent of the side chain rotation. The D154-R161 contact is extremely stable, while the E49-H131 contact is fluctuating due to competing interactions.

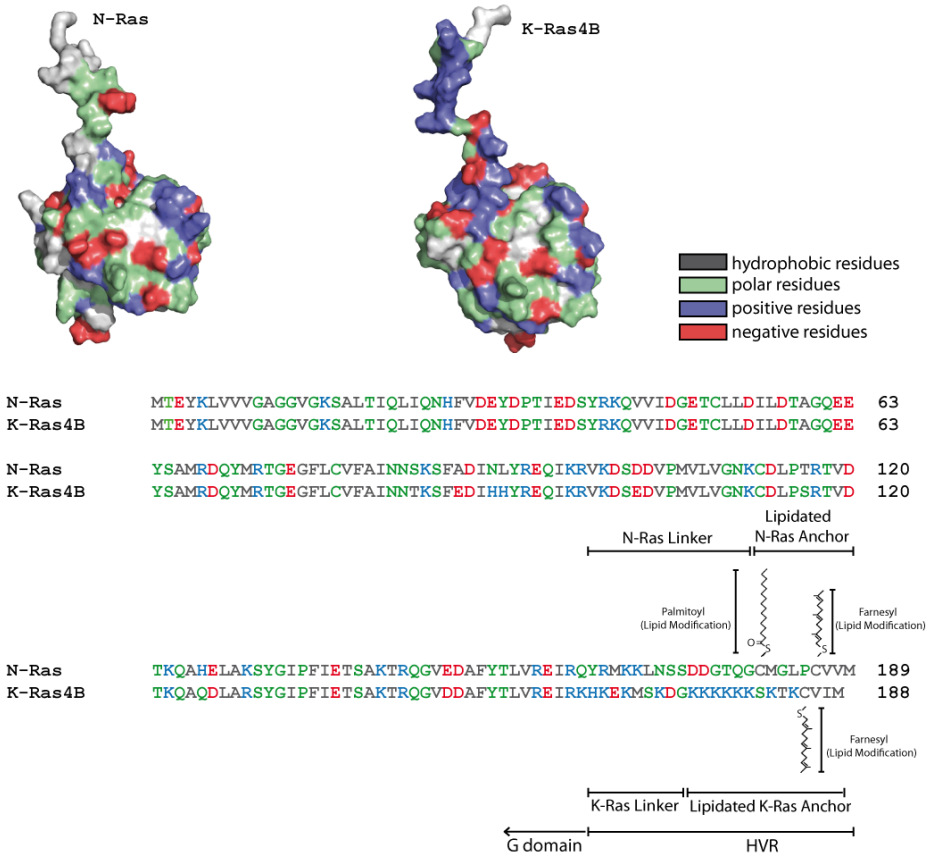

Fig. S10: Comparison of the surface localisation of hydrophobic, polar and charged residues between N-Ras and K-Ras4B. Shown is the surface formed by helices α4 and α5, as well as a sequence alignment with color coded residues (hydrophobic residues: gray, polar residues: green, positively charged residues: blue, negatively charged residues: red).

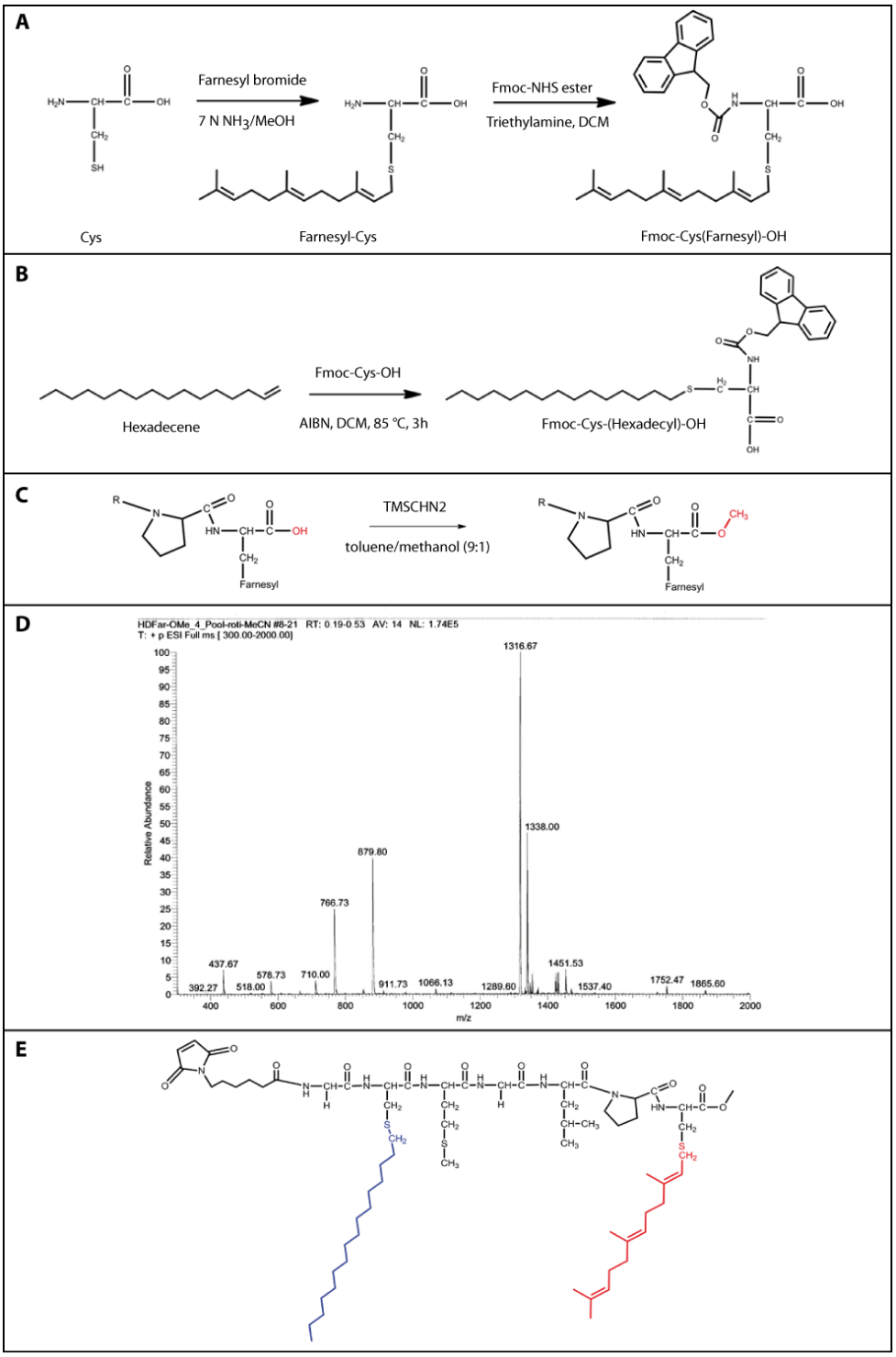

Figure S11: Lipid anchor synthesis for N-Ras. In **A** the coupling of cysteine with farnesyl bromide, which results in Fmoc-Cys(Farnesyl)-OH is shown. The radical reaction of hexadecane with Fmoc-Cys-OH, yielding Fmoc-Cys(Hexadecyl)-OH is shown in **B**. The last synthesis step was the methylation of the terminal carboxylic acid of the cysteine with trimethylsilyldiazomethane, which is displayed in **C**. The ESI-MS spectrum of the final product is shown in **D**. The complete structure of the synthesized peptide Maleimidocaproyl-Gly-Cys(Hexadecyl)-Met-Gly-Leu-Pro-Cys(Farnesyl)-OMethyl is shown in **E**. The Hexadecyl-moiety is labeled in blue and the Farnesyl-anchor in red.

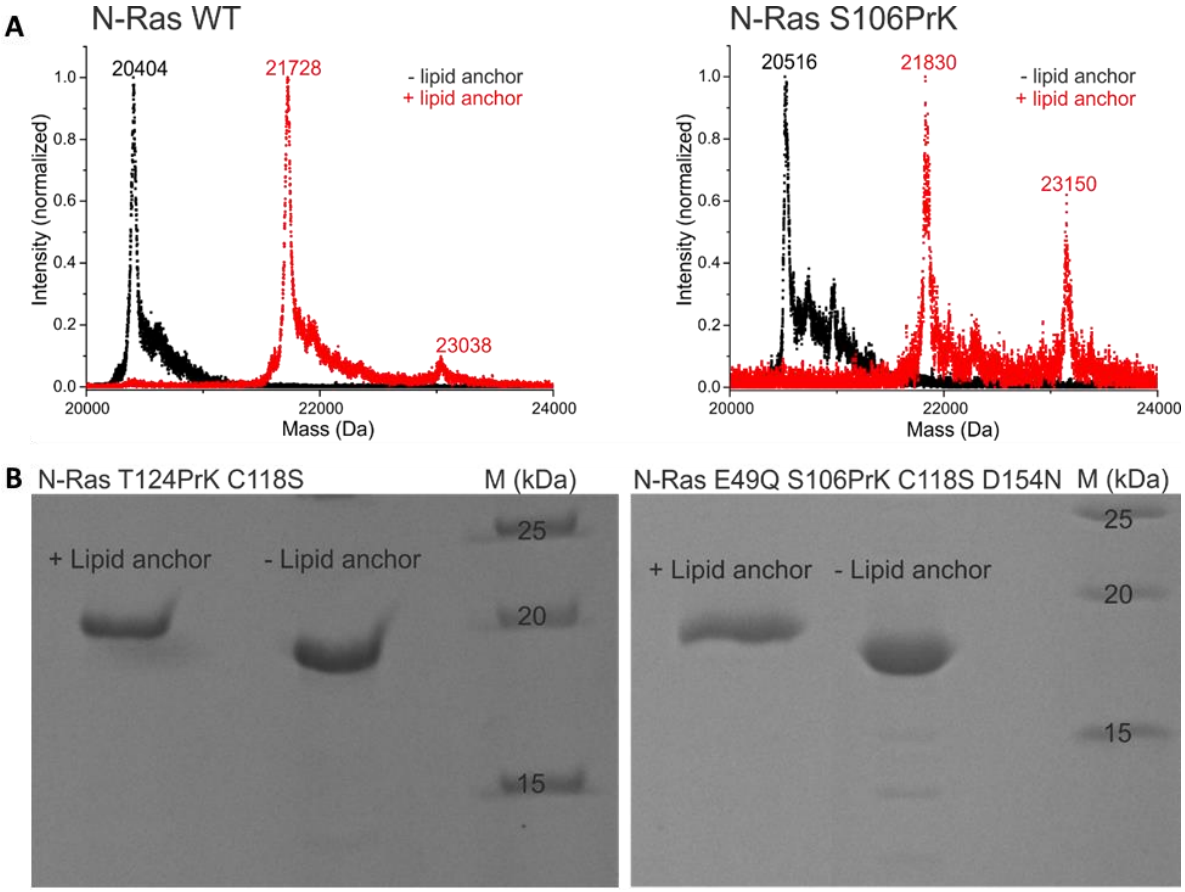

Fig. S12: N-Ras lipidation. In **A** the MADLI-MS results measured before and after N-Ras lipidation are shown. The lipid anchor exhibits a molecular mass of 1316 Da. For the wildtype, a mass difference of 1324 Da was observed after lipid coupling. For the N-Ras mutant S106PrK, a mass difference of 1314 Da was measured after lipid coupling. In **B** the SDS-PAGE gels for N-Ras T124PrK C118S and N-Ras E49Q S106PrK C118S D154N before and after lipid coupling are shown. A mass difference is observable due to the lipidation.

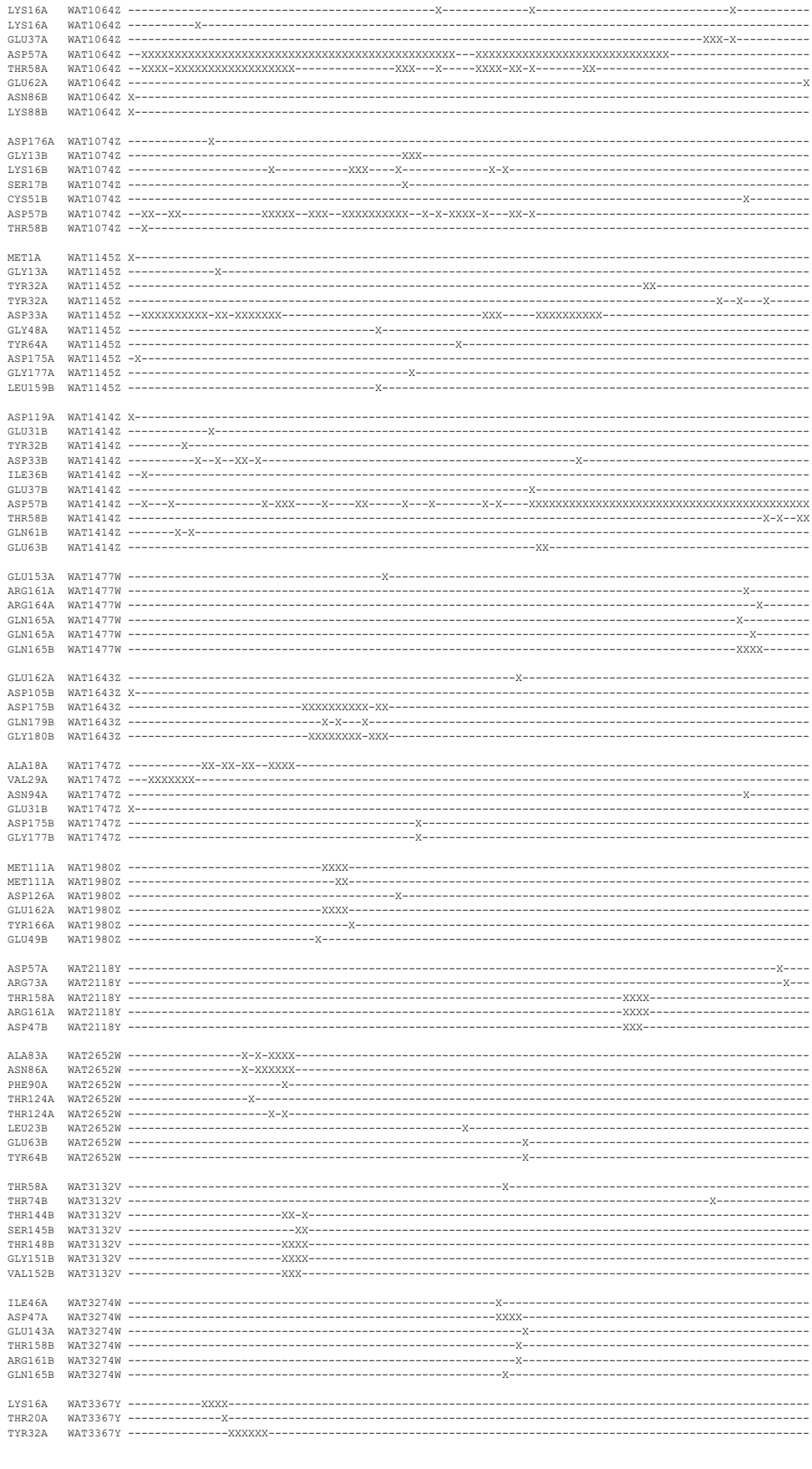
LYS16A WAT1064Z
LYS16A WAT1064Z
GLU37A WAT1064Z
ASP57A WAT1064Z
THR58A WAT1064Z
GLU62A WAT1064Z
ASN86B WAT1064Z
LYS88B WAT1064Z
ASP176A WAT1074Z
GLY13B WAT1074Z
LYS16B WAT1074Z
SER17B WAT1074Z
CYS51B WAT1074Z
ASP57B WAT1074Z
THR58B WAT1074Z
MET1A WAT1145Z
GLY13A WAT1145Z
TYR32A WAT1145Z
TYR32A WAT1145Z
ASP33A WAT1145Z
GLY48A WAT1145Z
TYR64A WAT1145Z
ASP175A WAT1145Z
GLY177A WAT1145Z
LEU159B WAT1145Z
ASP119A WAT1414Z
GLU31B WAT1414Z
TYR32B WAT1414Z
ASP33B WAT1414Z
ILE36B WAT1414Z
GLU37B WAT1414Z
ASP57B WAT1414Z
THR58B WAT1414Z
GLN61B WAT1414Z
GLU63B WAT1414Z
GLU153A WAT1477W
ARG161A WAT1477W
ARG164A WAT1477W
GLN165A WAT1477W
GLN165A WAT1477W
GLN165B WAT1477W
GLU162A WAT1643Z
ASP105B WAT1643Z
ASP175B WAT1643Z
GLN179B WAT1643Z
GLY180B WAT1643Z
ALA18A WAT1747Z
VAL29A WAT1747Z
ASN94A WAT1747Z
GLU31B WAT1747Z
ASP175B WAT1747Z
GLY177B WAT1747Z
MET111A WAT1980Z
MET111A WAT1980Z
ASP126A WAT1980Z
GLU162A WAT1980Z
TYR166A WAT1980Z
GLU49B WAT1980Z
ASP57A WAT2118Y
ARG73A WAT2118Y
THR158A WAT2118Y
ARG161A WAT2118Y
ASP47B WAT2118Y
ALA83A WAT2652W
ASN86A WAT2652W
PHE90A WAT2652W
THR124A WAT2652W
THR124A WAT2652W
LEU23B WAT2652W
GLU63B WAT2652W
TYR64B WAT2652W
THR58A WAT3132V
THR74B WAT3132V
THR144B WAT3132V
SER145B WAT3132V
THR148B WAT3132V
GLY151B WAT3132V
VAL152B WAT3132V
ILE46A WAT3274W
ASP47A WAT3274W
GLU143A WAT3274W
THR158B WAT3274W
ARG161B WAT3274W
GLN165B WAT3274W
LYS16A WAT3367Y
THR20A WAT3367Y
TYR32A WAT3367Y

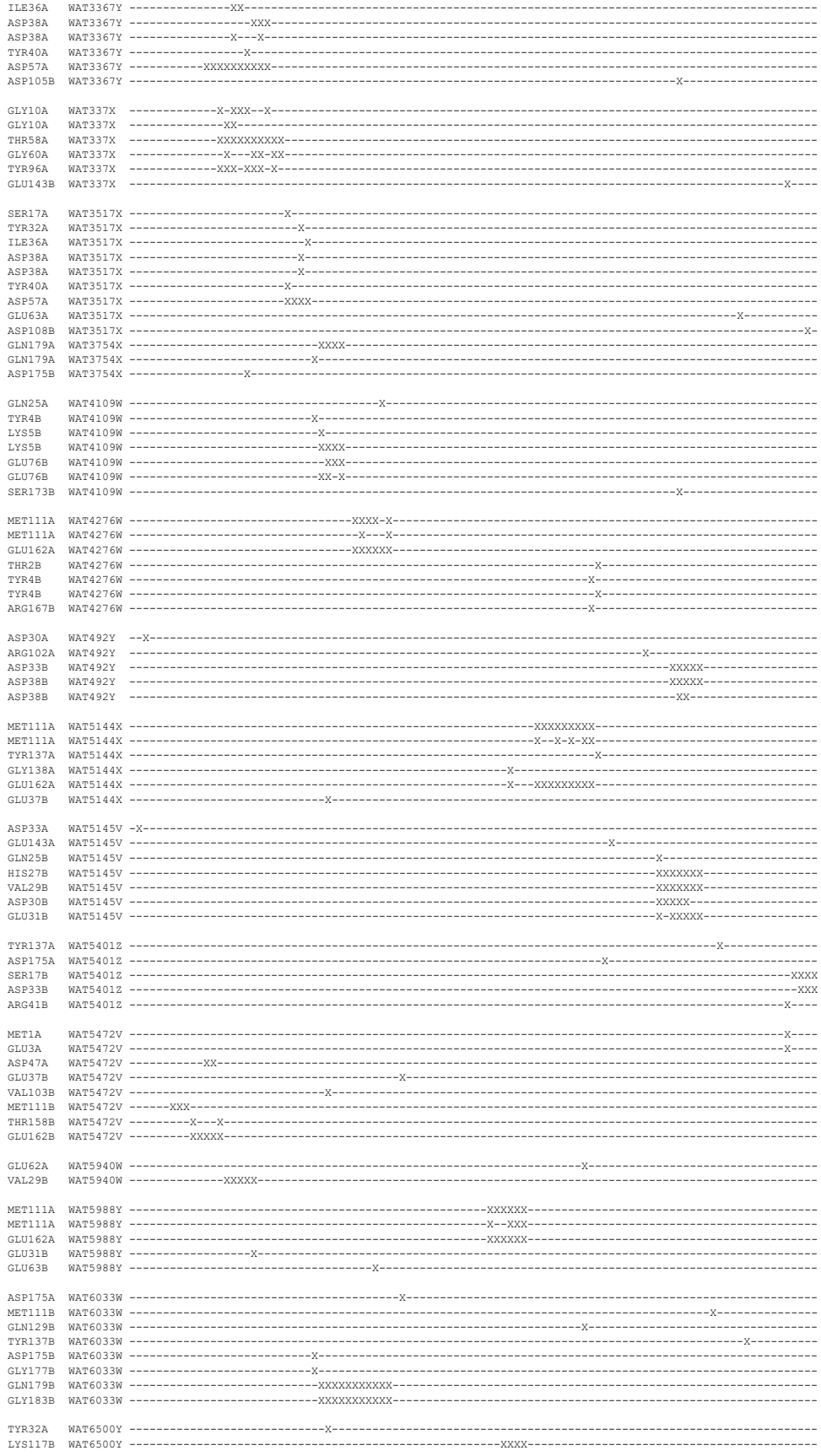
ILE36A WAT3367Y
ASP38A WAT3367Y
ASP38A WAT3367Y
TYR40A WAT3367Y
ASP57A WAT3367Y
ASP105B WAT3367Y
GLY10A WAT337X
GLY10A WAT337X
THR58A WAT337X
GLY60A WAT337X
TYR96A WAT337X
GLU143B WAT337X
SER17A WAT3517X
TYR32A WAT3517X
ILE36A WAT3517X
ASP38A WAT3517X
ASP38A WAT3517X
TYR40A WAT3517X
ASP57A WAT3517X
GLU63A WAT3517X
ASP108B WAT3517X
GLN179A WAT3754X
GLN179A WAT3754X
ASP175B WAT3754X
GLN25A WAT4109W
TYR4B WAT4109W
LYS5B WAT4109W
LYS5B WAT4109W
GLU76B WAT4109W
GLU76B WAT4109W
SER173B WAT4109W
MET111A WAT4276W
MET111A WAT4276W
GLU162A WAT4276W
THR2B WAT4276W
TYR4B WAT4276W
TYR4B WAT4276W
ARG167B WAT4276W
ASP30A WAT492Y
ARG102A WAT492Y
ASP33B WAT492Y
ASP38B WAT492Y
ASP38B WAT492Y
MET111A WAT5144X
MET111A WAT5144X
TYR137A WAT5144X
GLY138A WAT5144X
GLU162A WAT5144X
GLU37B WAT5144X
ASP33A WAT5145V
GLU143A WAT5145V
GLN25B WAT5145V
HIS27B WAT5145V
VAL29B WAT5145V
ASP30B WAT5145V
GLU31B WAT5145V
TYR137A WAT5401Z
ASP175A WAT5401Z
SER17B WAT5401Z
ASP33B WAT5401Z
ARG41B WAT5401Z
MET1A WAT5472V
GLU3A WAT5472V
ASP47A WAT5472V
GLU37B WAT5472V
VAL103B WAT5472V
MET111B WAT5472V
THR158B WAT5472V
GLU162B WAT5472V
GLU62A WAT5940W
VAL29B WAT5940W
MET111A WAT5988Y
MET111A WAT5988Y
GLU162A WAT5988Y
GLU31B WAT5988Y
GLU63B WAT5988Y
ASP175A WAT6033W
MET111B WAT6033W
GLN129B WAT6033W
TYR137B WAT6033W
ASP175B WAT6033W
GLY177B WAT6033W
GLN179B WAT6033W
GLY183B WAT6033W
TYR32A WAT6500Y
LYS117B WAT6500Y

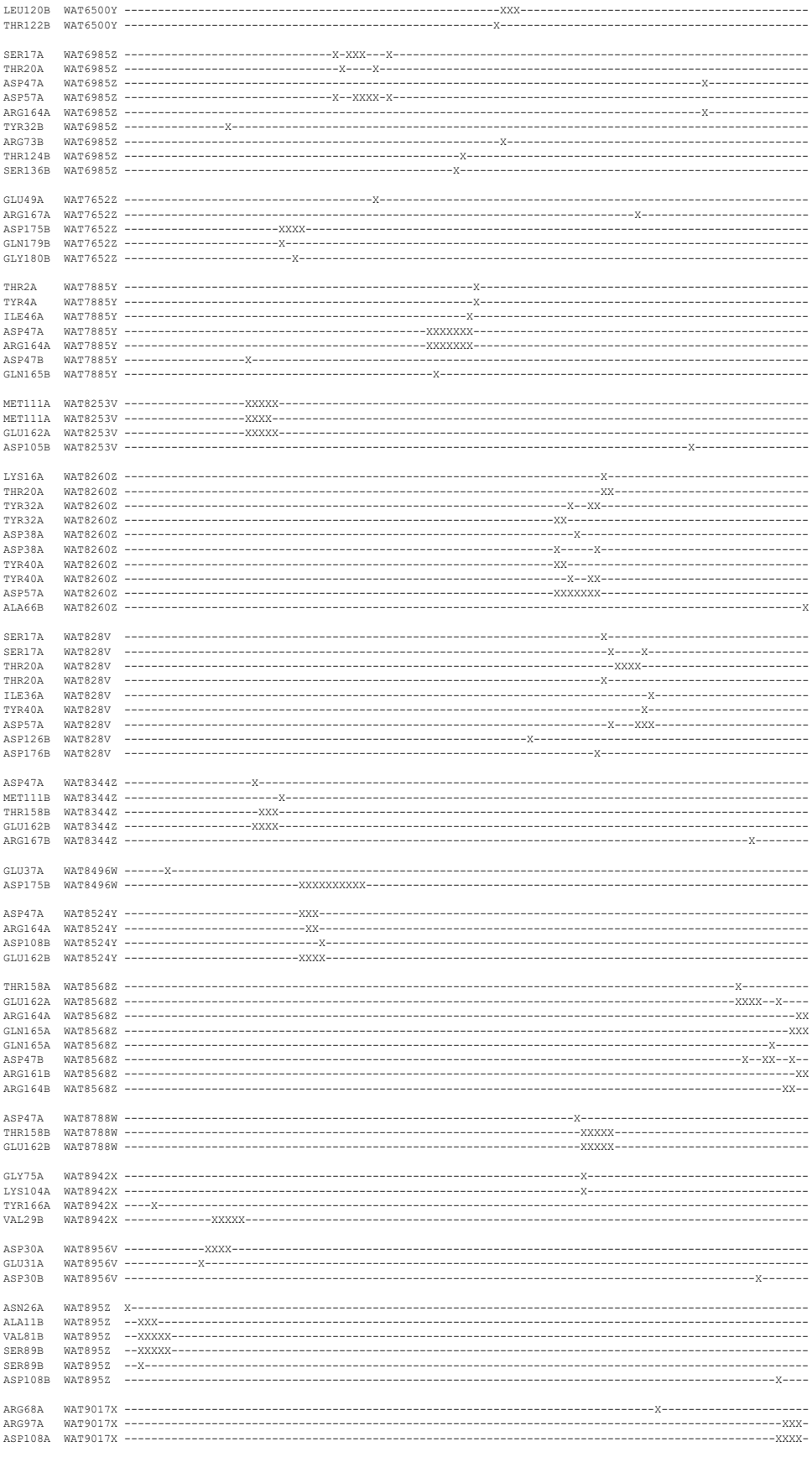
LEU120B WAT6500Y
THR122B WAT6500Y
SER17A WAT6985Z
THR20A WAT6985Z
ASP47A WAT6985Z
ASP57A WAT6985Z
ARG164A WAT6985Z
TYR32B WAT6985Z
ARG73B WAT6985Z
THR124B WAT6985Z
SER136B WAT6985Z
GLU49A WAT7652Z
ARG167A WAT7652Z
ASP175B WAT7652Z
GLN179B WAT7652Z
GLY180B WAT7652Z
THR2A WAT7885Y
TYR4A WAT7885Y
ILE46A WAT7885Y
ASP47A WAT7885Y
ARG164A WAT7885Y
ASP47B WAT7885Y
GLN165B WAT7885Y
MET111A WAT8253V
MET111A WAT8253V
GLU162A WAT8253V
ASP105B WAT8253V
LYS16A WAT8260Z
THR20A WAT8260Z
TYR32A WAT8260Z
TYR32A WAT8260Z
ASP38A WAT8260Z
ASP38A WAT8260Z
TYR40A WAT8260Z
TYR40A WAT8260Z
ASP57A WAT8260Z
ALA66B WAT8260Z
SER17A WAT828V
SER17A WAT828V
THR20A WAT828V
THR20A WAT828V
ILE36A WAT828V
TYR40A WAT828V
ASP57A WAT828V
ASP126B WAT828V
ASP176B WAT828V
ASP47A WAT8344Z
MET111B WAT8344Z
THR158B WAT8344Z
GLU162B WAT8344Z
ARG167B WAT8344Z
GLU37A WAT8496W
ASP175B WAT8496W
ASP47A WAT8524Y
ARG164A WAT8524Y
ASP108B WAT8524Y
GLU162B WAT8524Y
THR158A WAT8568Z
GLU162A WAT8568Z
ARG164A WAT8568Z
GLN165A WAT8568Z
GLN165A WAT8568Z
ASP47B WAT8568Z
ARG161B WAT8568Z
ARG164B WAT8568Z
ASP47A WAT8788W
THR158B WAT8788W
GLU162B WAT8788W
GLY75A WAT8942X
LYS104A WAT8942X
TYR166A WAT8942X
VAL29B WAT8942X
ASP30A WAT8956V
GLU31A WAT8956V
ASP30B WAT8956V
ASN26A WAT895Z
ALA11B WAT895Z
VAL81B WAT895Z
SER89B WAT895Z
SER89B WAT895Z
ASP108B WAT895Z
ARG68A WAT9017X
ARG97A WAT9017X
ASP108A WAT9017X

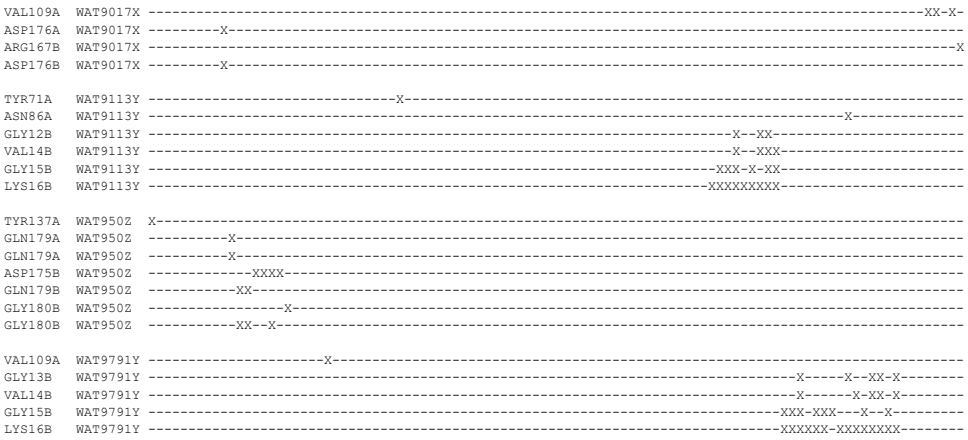

Fig. S13: Water-Protein contact analysis for simulation I.9. Water molecules forming a hydrogen bond to one of the two Ras proteins at any time of the simulation trajectory I.9 are shown. Every block displays the analysis for one water molecule. The first and second columns specify the residues in contact. An X represents an existing contact in this simulation frame. A simultaneous contact to both chains means that the water molecule is directly bridging the dimer interface.

Supplementary Tables

Table S1: Categorization of the dimer structural model obtained by protein-protein docking.

Category	Number	Interface
I	12	α4/α5 - α4/α5
II	6	α3/α4 – α3/α4
III	121	β-sheet – β-sheet
IV	3	α3/α4 - β-sheet
V	3	α4/α5 - β-sheet
VI	2	α5 - β-sheet
VII	1	α4 – α4
VIII	2	α2/α5 – α2/α5
IX	28	Involvement of nucleotide Binding pocket
Total	178	

Table S2: FRET and EPR results. The table shows the obtained donor's lifetimes with and without the acceptor, the calculated and corrected FRET efficiencies as well as the distances between the fluorophores coupled to lipidated Ras on POPC liposomes or in solution. Displayed are mean values, the standard deviation is displayed only for the final distance. Also shown is the result of the EPR measurements and the FRET GDP-GDP distance published by Güldenhaupt et al.[1]

Label	Membrane (POPC)	Lifetime without acceptor / ns	Lifetime with acceptor / ns	Corr. Efficiency	Distance (Å)
106-Atto532-106-Atto655	yes	1.87	1.28	~ 79 %	43.3 ± 2.3
124-Atto532-124-Atto655	yes	2.66	2.53	~ 15 %	72.0 ± 3.5
124-Proxyl-124-Proxyl	yes				59.0 ± 2.5
GDP-MANT-GDP-TNP	yes	5.5	4.9	~ 28 %	46.3 ± 1.4
106-Atto532-106-Atto655	no	1.86	1.41	~ 60 %	49.7 ± 0.8
124-Atto532-124-Atto655	no	3.56	3.44	~ 10 %	77.0 ± 0.5
106-Atto532-106-Atto655 E49Q D154N	yes	3.13	3.24	~ 0 %	

Table S3: Validation of Ras dimer structural models by comparing theoretical distances with experimental values. Given as reference are the three experimental distances, obtained by FRET experiments for the FRET fluorophore pairs S106-Atto532/S106-Atto655, T124-Atto532/T124-Atto655, GDP-MANT/GDP-TNP and the EPR label pair T124-Proxyl/T124-Proxyl taken from Fig. 3. Summarized are the mean values and the standard deviation of the gauss fit of the calculated distance distribution of the four aforementioned label for all obtained dimer structural models from protein-protein docking server (see Supporting Note 2) using the mtsslWizard[21] in PyMol as shown in Fig. S3 and described in Supporting Note 6. The agreement with the experiment is color coded in the following manner; green: the calculated mean distance is within the standard deviation of the experimental value; yellow: the calculated standard deviation is within the experimental standard deviation; red: the calculated values are not in accordance with the experiment. Based on these results, the dimer conformations I.5 to I.12 where chosen for further refinement through MD simulations. The categories are defined in the following manner based on their interaction sides, whereby categories I-III are found in the literature: **I** (contact between the surfaces formed by helices α4 and α5, **II** (contact between the surfaces formed by helices α3 and α4), **III** (contact between the surfaces formed by the beta sheets), **IV** (contact between helices α3 and α4 of one monomer with the beta sheet of the other monomer), **V** (contact between the helices α4 and α5 of one monomer with the beta sheet of the other monomer), **VI** (contact between the surfaces formed by helix α5 and the beta sheet), **VII** (contact between the surfaces formed by helices α4), **VIII** (contact between the surfaces formed by the helices α2 and α5), IX (involvement of the switch regions of at least one monomer in the dimer interface).

Conformation	Number of Structures	Distance / Å			
		S106-S106	T124-T124	T124-T124 Proxyl	Nucleotide - Nucleotide
Experimental		43,3 ± 2.3	72,0 ± 3.5	59.7 ± 2.5	46,3 ± 1,4
I.1	ref.[9]	39,2 ± 15,5	75,0 ± 8,6	57.5 ± 4.6	43,7 ± 2,2
I.2	ref.[9]	36.1 ± 16.9	76.4 ± 10.2	59.1 ± 4.3	49.3 ± 2.2
I.3	ref.[12]	48.7 ± 12.5	39.2 ± 15.0	27.2 ± 3.5	46.2 ± 2.6
I.4	ref.[12]	53.0 ± 10.5	66.0 ± 9.9	45.5 ± 4.4	39.6 ± 2.1
I.5	1	28.4 ± 13.4	72.4 ± 10.1	56.2 ± 4.3	44.2 ± 2.5
I.6	1	31.8 ± 14.6	76.36 ± 8.9	56.6 ± 4.4	44.99 ± 2.2
I.7	1	35.8 ± 15.0	77.1 ± 9.1	57.4 ± 4.3	43.1 ± 1.8
I.8	1	31.1 ± 13.1	73.0 ± 9.2	54.8 ± 4.3	45.1 ± 2.0
I.9	1	32.3 ± 13.0	71.4 ± 10.7	54.1 ± 4.1	42.9 ± 2.6
I.10	1	27.1 ± 12.6	72.7 ± 10.8	54.7 ± 4.2	46.0 ± 2.5
I.11	1	26.9 ± 12.9	74.8 ± 10.1	55.8 ± 4.5	48.63 ± 2.4
I.12	1	45.1 ± 15.4	75.2 ± 9.1	56.1 ± 4.0	38.7 ± 2.5
I.13	1	26.5 ± 12.9	78.7 ± 8.8	58.8 ± 4.4	49.9 ± 2.4
I.14	1	23.6 ± 11.5	76.9 ± 9.8	58.1 ± 4.4	50.8 ± 2.4
I.15	1	64.7 ± 12.6	57.3 ± 11.6	40.4 ± 3.7	30.8 ± 2.3
I.16	1	67.9 ± 12.9	59.1 ± 10.1	41.2 ± 3.6	35.5 ± 2.5
II.1	ref.[13]	24.5 ± 10.9	25.8 ± 10.9	12.0 ± 3.3	47.6 ± 3.0
II.2	ref.[14]	39.3 ± 11.7	46.8 ± 11.1	28.3 ± 4.4	53.6 ± 3.1
II.3	5	20.8 ± 10.3	24.9 ± 12.0	13.9 ± 3.8	46.6 ± 3.0
II.4	1	36.4 ± 12.1	47.7 ± 12.4	30.6 ± 4.7	54.4 ± 3.1
III.1	ref.[14]	42.1 ± 15.4	70.7 ± 13.6	59.7 ± 3.9	22.8 ± 2.6
III.2	29	54.4 ± 16.5	67.1 ± 14.9	55.1 ± 3.7	21.2 ± 2.6
III.3	18	70.9 ± 13.2	62.2 ± 14.5	52.5 ± 3.9	17.2 ± 2.9

III.4	18	68.4 ± 14.0	62.2 ± 14.9	52.0 ± 3.7	17.1 ± 2.9
III.5	3	62.8 ± 15.2	80.9 ± 12.2	65.9 ± 3.7	34.7 ± 2.6
III.6	2	66.3 ± 15.0	75.0 ± 11.7	60.5 ± 3.5	26.1 ± 3.0
III.7	4	54.3 ± 16.0	63.7 ± 13.9	53.4 ± 3.7	20.0 ± 2.7
III.8	6	76.8 ± 14.2	77.4 ± 11.2	62.0 ± 3.7	32.5 ± 2.3
III.9	1	65.1 ± 13.3	60.3 ± 16.3	54.9 ± 3.4	20.1 ± 2.7
III.10	2	70.1 ± 14.8	73.6 ± 11.5	58.1 ± 3.9	22.0 ± 2.7
III.11	1	67.8 ± 16.2	69.5 ± 13.0	55.0 ± 4.0	25.1 ± 1.9
III.12	2	50.8 ± 14.6	71.2 ± 13.7	57.5 ± 3.3	21.0 ± 3.0
III.13	2	73.0 ± 11.7	82.6 ± 10.4	65.9 ± 3.6	31.5 ± 3.1
III.14	3	57.1 ± 15.3	75.4 ± 11.6	58.9 ± 3.7	23.3 ± 3.0
III.15	1	51.9 ± 18.5	72.9 ± 11.2	56.8 ± 3.5	22.9 ± 2.6
III.16	1	49.7 ± 11.9	78.2 ± 12.8	63.7 ± 3.2	30.0 ± 3.5
III.17	1	60.6 ± 15.9	62.0 ± 13.9	53.0 ± 3.5	19.5 ± 2.5
III.18	2	58.8 ± 14.4	78.5 ± 10.4	61.5 ± 3.6	26.1 ± 2.7
III.19	2	77.6 ± 12.2	78.8 ± 11.6	62.2 ± 3.4	31.8 ± 2.5
III.20	1	66.2 ± 11.8	75.0 ± 12.4	61.8 ± 3.2	34.4 ± 2.6
III.21	3	50.0 ± 16.3	97.3	80.0 ± 3.8	56.8 ± 2.5
III.22	8	66.6 ± 9.2	70.4 ± 11.2	51.3 ± 4.1	45.6 ± 3.3
III.23	1	49.8 ± 11.2	83.2 ± 13.2	67.1 ± 3.4	33.0 ± 3.2
III.24	1	31.8 ± 14.3	86.2 ± 9.9	69.3 ± 4.2	64.0 ± 2.5
III.25	2	19.5 ± 9.4	71.9 ± 10.5	53.2 ± 4.5	52.2 ± 2.1
III.26	1	61.5 ± 14.0	52.0 ± 13.8	39.3 ± 4.0	31.1 ± 2.3
III.27	1	77.8 ± 12.1	55.8 ± 15.3	46.3 ± 3.7	29.6 ± 2.1
III.28	1	76.7 ± 10.8	77.6 ± 13.0	65.8 ± 3.9	84.5 ± 11.4
III.29	2	62.7 ± 11.8	66.3 ± 13.8	56.7 ± 4.2	38.4 ± 2.4
III.30	1	105.3 ± 14.8	57.0 ± 9.7	37.3 ± 3.6	17.9 ± 3.3
III.31	1	59.3 ± 13.9	55.4 ± 9.9	36.3 ± 3.2	12.1 ± 2.3
IV.1	1	53.3 ± 9.7	69.4 ± 13.5	60.0 ± 3.7	51.9 ± 3.4
IV.2	1	53.3 ± 12.9	78.1 ± 11.2	63.4 ± 3.5	39.5 ± 2.7
IV.3	1	26.8 ± 13.8	41.0 ± 16.9	40.9 ± 3.5	40.4 ± 2.4
V.1	2	55.2 ± 10.9	82.8 ± 14.5	67.6 ± 3.5	34.9 ± 2.9
V.2	1	25.4 ± 11.7	43.4 ± 15.7	35.8 ± 3.5	40.0 ± 3.3
VI.1	1	32.8 ± 11.6	48.2 ± 10.6	30.8 ± 4.3	43.4 ± 2.6
VII.1	1	81.1 ± 9.2	67.9 ± 9.8	49.7 ± 4.4	38.1 ± 2.3
VIII.1	2	48.9 ± 11.2	43.0 ± 14.5	35.5 ± 3.3	44.9 ± 3.5
IX.1	1	67.5 ± 10.2	69.1 ± 10.3	51.2 ± 4.2	45.5 ± 3.2
IX.2	14	33.9 ± 12.4	88.8 ± 11.2	72.1 ± 3.5	44.8 ± 2.7
IX.3	1	59.4 ± 14.1	57.2 ± 16.0	51.5 ± 3.8	25.4 ± 2.1

IX.4	1	65.8 ± 10.6	89.9 ± 14.3	72.2 ± 3.7	46.8 ± 2.9
IX.5	2	77.5 ± 11.7	69.7 ± 14.5	68.2 ± 3.7	84.3 ± 12.4
IX.6	1	36.3 ± 13.9	33.3 ± 14.5	29.8 ± 4.2	33.8 ± 1.8
IX.7	2	48.2 ± 13.4	29.6 ± 12.3	26.7 ± 3.5	24.0 ± 2.6
IX.8	1	73.9 ± 11.9	33.7 ± 12.8	28.4 ± 3.4	25.0 ± 2.5
IX.9	1	73.8 ± 11.7	34.7 ± 12.9	29.4 ± 3.4	26.2 ± 3.2
IX.10	1	78.5 ± 11.3	44.2 ± 14.2	32.4 ± 3.0	13.2 ± 2.9
IX.11	1	77.6 ± 13.4	53.6 ± 9.4	34.1 ± 3.5	10.4 ± 2.7
IX.12	2	80.8 ± 10.9	43.7 ± 15.4	34.2 ± 3.5	14.5 ± 1.9

Table S4: Comparison of NMR derived distances of a K-Ras4B-GDP dimer from Lee et al[2] with the dimer models shown in Fig. 1. Lee et al. constructed a K-Ras4B GDP dimer model based on NMR derived distance data (Model I.3 in Fig. 1). We compared all other dimer models shown in Fig. 1, using the same procedure described by Lee et al. Cells marked in green are in accordance with the experimental distances. The distance measurements involving residue 169 were not possible for model II.2, as it is only modelled from residue 1-167.

Residue	Atom	Residue	Atom	PRE Distance / Å	I.1	I.2	I.3	I.4	II.1	II.2	III.1
118	SG	112	CG1/CG2	15.3 ± 3,0	19,6	23,9	18,2	17,1	32,1	30,5	38,8
118	SG	113	CD1/CD2	14.9 ± 3,0	26,0	30,4	15,8	20,5	21,3	24,6	41,7
118	SG	114	CG1/CG2	17.5 ± 3,0	21,3	26,1	18,7	17,1	30,6	31,2	35,8
118	SG	125	CG1/CG2	16.1 ± 3,0	31,0	34,8	16,2	22,8	20,6	23,2	42,8
118	SG	133	CD1/CD2	14.6 ± 3,0	30,2	34,2	16,2	24,3	21,1	19,6	45,4
118	SG	139	CD1	15.0 ± 3,0	28,6	31,9	18,0	23,3	30,9	28,8	48,0
118	SG	142	CD1	14.4 ± 3,0	20,2	24,7	16,8	13,8	37,3	34,7	43,6
118	SG	128	N	13.1 ± 3,0	31,6	35,5	10,3	20,9	25,5	24,7	52,9
118	SG	127	CG2	13.2 ± 3,0	28,0	34,7	10,8	17,6	29,0	28,2	50,5
118	SG	142	CG2	14.7 ± 3,0	20,4	26,0	17,3	13,1	36,8	35,8	42,4
169	CG	45	CG1/CG2	15.5 ± 3,0	27,2	23,5	12,7	29,7	45,9		43,1
169	CG	46	CD1	15.5 ± 3,0	24,8	21,5	13,5	27,3	44,3		46,8
169	CG	159	CD1/CD2	16.1 ± 3,0	19,0	16,2	17,0	19,8	31,0		40,4
169	CG	160	CG1/CG2	14.5 ± 3,0	20,5	16,8	11,8	22,4	36,5		40,9
169	CG	163	CD1	15.5 ± 3,0	20,1	17,4	16,8	23,2	35,7		44,2
169	CG	165	N	14.8 ± 3,0	16,8	10,6	11,9	18,6	37,1		51,4
169	CG	167	N	15.3 ± 3,0	18,3	10,7	14,9	19,2	34,6		49,6
169	CG	169	N	14.8 ± 3,0	16,7	7,1	15,4	17,4	34,9		53,6
169	CG	172	N	16.1 ± 3,0	20,4	9,2	18,2	19,4	35,0		55,0

Table S5: Comparison of NMR derived distances of a K-Ras4B-GTP dimer from Lee et al.[2] with the dimer models shown in Fig. 1. Lee et al. constructed a K-Ras4B GTP dimer model based on NMR derived distance data (Model I.4 in Fig. 1). We compared all other dimer models shown in Fig. 1, using the same procedure described by Lee et al. Cells marked in green are in accordance with the experimental distances. The distance measurements involving residue 169 were not possible for model II.2, as it is only modeled from residue 1-167.

Residue	Atom	Residue	Atom	PRE Distance / Å	I.1	I.2	I.3	I.4	II.1	II.2	III.1
118	SG	44	CG1/CG2	15,4 ± 3,0	12,1	16,6	29.0	18,0	44,3	43,6	30,4
118	SG	45	CG1/CG2	14,4 ± 3,0	7,9	12,2	31.3	17,1	48,9	46,7	33,9
118	SG	46	CD1	15,7 ± 3,0	13,1	18,4	29.5	18,5	47,5	45,4	38,5
118	SG	142	CD1	13,3 ± 3,0	20,2	24,7	16.8	13,9	37,3	34,7	43,6
118	SG	160	CG1/CG2	16,0 ± 3,0	14,5	18,9	25.3	18,6	40,6	38,8	35,5
118	SG	127	CG2	15,2 ± 3,0	28,0	32,4	10.8	17,6	29,0	28,2	50,5
118	SG	142	CG2	13,8 ± 3,0	20,4	25,2	17.3	13,1	36,8	35,8	42,4
118	SG	144	CG2	13,7 ± 3,0	21,5	27,5	20.1	15,2	36,7	37,2	39,2
118	SG	148	CG2	14,4 ± 3,0	22,7	29,6	24.7	17,1	40,9	43,2	36,6
169	CG	113	CD1/CD2	15,9 ± 3,0	16,0	17,6	24.4	15,8	28,4		47,1
169	CG	125	CG1/CG2	16,0 ± 3,0	21,3	24,4	30.9	19,9	31,0		50,1
169	CG	133	CD1/CD2	13,5 ± 3,0	15,1	18,2	27.5	14,1	24,7		49,1
169	CG	139	CD1	15,2 ± 3,0	14,3	12,2	23.7	15,1	30,2		52,2
169	CG	128	N	15,9 ± 3,0	19,2	23,9	31.8	18,9	37,7		62,2
169	CG	176	N	17,1 ± 3,0	16,6	17,8	25.5	16,4	30,2		58,6
169	CG	177	N	17,5 ± 3,0	18,9	21,3	26.3	17,1	32,0		57,0
169	CG	178	N	17,2 ± 3,0	21,6	24,0	27.7	17,7	34,1		57,6
169	CG	179	N	17,2 ± 3,0	24,5	26,4	28..6	18,9	37,3		58,1

Table S6: Summary of the MD simulation systems. Row one gives the dimer conformations according to the numbering in Table S3 that are used to initiate MD simulations to obtain an equilibrated structure. Also given are the numbers of the run with the same conformation but different start velocity distribution (row two), the simulation time in nano seconds (row three), and the composition of the simulation system.

Conformation	Run	Simulation Time	Total Atoms	Protein Atoms	Membrane Atoms	Water Molecules	Na^+	Cl^-
I.1	I	550 ns	234868	5942	26468	50502	243	207
I.5	I	550 ns	234552	5942	26520	50410	243	207
I.6	I	800 ns	234668	5942	26468	50452	243	207
I.7	I	800 ns	260244	5942	26468	56846	243	207
I.8	I	550 ns	234664	5942	26520	50438	243	207
I.9	I	800 ns	234860	5942	26468	50500	243	207
I.10	I	550 ns	234664	5942	26520	50438	243	207
I.11	I	550 ns	232964	5942	26624	49.987	243	207
I.12	I	550 ns	234916	5942	26468	50514	243	207

Table S7: Validation of the representative Ras dimer structures from the 9 simulation runs by comparing theoretical distances with experimental values. Given as reference are the three experimental distances, obtained by FRET experiments for the FRET fluorophore pairs S106-Atto532/S106-Atto655, T124-Atto532/T124-Atto655, GDP-MANT/GDP-TNP and the EPR label pair T124-Proxyl/T124-Proxyl taken from Fig. 3. Summarized are the mean values and their standard deviation of the gauss fit of the calculated distance distribution of the four aforementioned label for all obtained representative structural models from the simulation runs (see Supporting Note 6) using the mtsslWizard[21] as shown in Fig. S3 and described in Supporting Note 5. The agreement with the experiment is color coded in the following manner; green: the calculated mean distance is within the standard deviation of the experimental value; yellow: the calculated standard deviation is within the experimental standard deviation; red: the calculated values are not in accordance with the experiment.

	Distance / Å			
Conformation	**S106-S106**	**T124-T124**	**T124-T124 Proxyl**	**Nucleotide - Nucleotide**
Experimental	43,3 ± 2.3	72,0 ± 3.5	59.7 ± 2.5	46,3 ± 1,4
I.1	47.0 ± 11.3	81.5 ± 10.7	63.8 ± 4.3	58.3 ± 2.4
I.5	40,1 ± 11,6	79,9 ± 10,1	63.7 ± 4.5	52,5 ± 2,1
I.6	42,5 ± 9,9	80,5 ± 9,9	61.6 ± 4.4	56,4 ± 2,4
I.7	45,2 ± 14,7	82,1 ± 9,3	62.7 ± 4.5	55,1 ± 2,4
I.8	47,4 ± 12,6	79,3 ± 9,2	60.1 ± 4.2	51,0 ± 2,2
I.9	41,1 ± 11,5	76,5 ± 10,6	58.8 ± 4.2	43,6 ± 1,9
I.10	39,5 ± 9,5	78,3 ± 10,1	60.3 ± 4.2	45,8 ± 1,9
I.11	40.4 ± 11.8	62.7 ± 11.3	46.4 ± 4.0	51.2 ± 2.1
I.12	45,6 ± 16,2	80,7 ± 9,7	62.6 ± 4.4	37,8 ± 2,0

Table S8: Summary of the N-Ras dimer interface. Summarized is the contact analysis of nine independent MD simulation runs (see Fig. S5). For every intermolecular contact it is specified in how many simulations it is present, and whether it is a hydrogen bond/salt bridge or van der waals contact. Finally, it is shown in how many simulations the contact is present one sided and in how many it is present two sided. Only contacts that are present in the last third of the simulation are included.

		Number of simulations present at least one sided		**Number of simulations present Two sided**	
Contact		h-bond/salt bridge	Van der waals	h-bond/salt bridge	Van der waals
D154	R161	8	0	3	0
E49	H131	2	3	0	0
R161	E162	3	0	0	0
T158	R161	1	3	0	1
S136	N172	2	1	0	0
E162	Q165	2	1	0	0
E132	R164	2	0	0	0
R149	E153	2	0	0	0
E162	R164	2	0	0	0
G138	K169	1	4	0	1
R97	D175	2	0	0	0
H131	M168	0	3	0	0
D154	Y157	0	2	0	1
V45	Q150	1	1	1	0
E49	K128	1	1	0	0
L23	R149	1	0	0	0
D47	F141	1	0	0	0
D47	D154	1	0	0	0
G138	R164	1	0	0	0
G151	Y157	1	0	0	0
H131	K169	1	0	0	0
N172	N172	1	0	0	0
D108	Q165	1	0	0	0
V109	Q165	1	0	0	0
S136	S173	1	0	0	0
G138	R161	1	0	0	0
E132	R167	1	0	0	0
K169	T178	1	0	0	0
N172	E180	1	0	0	0
K135	Q165	0	3	0	0
K135	L171	0	3	0	0
S136	L171	0	3	0	0

P140	Q165	0	2	0	0
Q165	Q165	0	2	0	0
P140	R161	0	1	0	0
I139	M168	0	1	0	0
Y137	L171	0	1	0	0
G138	L171	0	1	0	0
Y137	N172	0	1	0	0
K135	R164	0	1	0	0
D108	D175	0	1	0	0
D108	D178	0	1	0	0
Y166	M182	0	1	0	0
K135	R167	0	1	0	0
K135	M168	0	1	0	0
K169	M182	0	1	0	0
K170	M182	0	1	0	0

Table S9: Final concentrations for the CuAAC. The table shows the final concentrations for the click-chemistry in order to attach the fluorophores to the protein.

Nr.	Substance	Concentration (µM)
1	$CuSO_4$	100
2	THPTA	50
3	Sodium ascorbate	2500
4	N-Ras S106-PrK / T124-PrK C118S	24
5	Atto532-azid / Atto655-azid	100
6	Benzoic acid	20

Table S10: Labelling efficiencies. The table shows the final labelling efficiencies of the click-chemistry with the fluorophores Atto532azide and Atto655azide.

Protein	Label
N-Ras S106-PrK	40 % Atto532azide
	40 % Atto655azide
N-Ras T124-PrK C118S	56 % Atto532azide
	41 % Atto655azide
Lipidated N-Ras S106-PrK	40 % Atto532azide
	57 % Atto655azide
Lipidated N-Ras T124-PrK C118S	47 % Atto532azide
	41 % Atto655azide
Lipidated N-Ras E49Q S106-PrK C118S D154N	37 % Atto532azide
	59 % Atto655azide

Table S11: PDB structures used as a starting point for the construction of dimer models.

PDB-ID	Isoform	Nucleotide/Analogon	Residues	Missing Residues	Residues with Missing Atoms
1ctq [1]	H-Ras	GppNHp	1-166	167-172	--
1q21 [2]	H-Ras	GDP	1-171	172	--
4q21 [3]	H-Ras	GDP	1-168	169-172	--
5ocg [4]	K-Ras4B	GppNHp	1-172	--	E31, R41
4l8g [5]	K-Ras4B	GDP	1-59, 70-167	60-69, 168-172	Q70, Y71, K128
5uhv [6]	N-Ras	GppNHp	1-166	167-172	E31, Q61, E62, E63, S65, Q70, Y71, R73, Q99, D126, K128, K135
3con [7]	N-Ras	GDP	1-60, 72-167	61-71, 168-172	E3, K5, R41, R73, D108, K128, E143, Q165

Table S12: Composition of the detected TCSPC fluorescence signal. The table displays the fraction of the detected total fluorescence signal that can undergo FRET.

Dimer	Probability	Fluorescence	„Fluorescence amount“	FRET	„FRET amount“
DD	0.014	2	0.028	0	0
DA	0.048	1	0.048	1	0.048
AD	0.048	1	0.048	1	0.048
AA	0.159	0	0	0	0
XX	0.231	0	0	0	0
XD	0.057	1	0.057	0	0
DX	0.057	1	0.057	0	0
XA	0.192	0	0	0	0
AX	0.192	0	0	0	0
Sum	**1**		**0.238**		**0.096**

Literature Cited

1. Güldenhaupt J, Rudack T, Bachler P, Mann D, Triola G, Waldmann H et al. N-Ras forms dimers at POPC membranes. Biophys J 2012; 103(7):1585–93.

2. Lee K-Y, Fang Z, Enomoto M, Gasmi-Seabrook G, Le Zheng, Koide S et al. Two Distinct Structures of Membrane-Associated Homodimers of GTP- and GDP-Bound KRAS4B Revealed by Paramagnetic Relaxation Enhancement. Angewandte Chemie (International ed. in English) 2020; 59(27):11037–45.

3. Muratcioglu S, Chavan TS, Freed BC, Jang H, Khavrutskii L, Freed RN et al. GTP-Dependent K-Ras Dimerization. Structure (London, England : 1993) 2015; 23(7):1325–35.

4. Prakash P, Sayyed-Ahmad A, Cho K-J, Dolino DM, Chen W, Li H et al. Computational and biochemical characterization of two partially overlapping interfaces and multiple weak-affinity K-Ras dimers. Sci Rep 2017; 7(1):40109. Available from: URL: https://www.nature.com/articles/srep40109.

5. Lyskov S, Gray JJ. The RosettaDock server for local protein-protein docking. Nucleic acids research 2008; 36(Web Server issue):W233-8.

6. Baspinar A, Cukuroglu E, Nussinov R, Keskin O, Gursoy A. PRISM: a web server and repository for prediction of protein-protein interactions and modeling their 3D complexes. Nucleic acids research 2014; 42(Web Server issue):W285-9.

7. Eswar N, Webb B, Marti-Renom MA, Madhusudhan MS, Eramian D, Shen M-Y et al. Comparative protein structure modeling using Modeller. Curr Protoc Bioinformatics 2006; Chapter 5:Unit-5.6.

8. Güldenhaupt J, Adigüzel Y, Kuhlmann J, Waldmann H, Kötting C, Gerwert K. Secondary structure of lipidated Ras bound to a lipid bilayer. The FEBS journal 2008; 275(23):5910–8.

9. Thapar R, Williams JG, Campbell SL. NMR characterization of full-length farnesylated and non-farnesylated H-Ras and its implications for Raf activation. Journal of molecular biology 2004; 343(5):1391–408.

10. Reuther G, Tan K-T, Köhler J, Nowak C, Pampel A, Arnold K et al. Structural model of the membrane-bound C terminus of lipid-modified human N-ras protein. Angewandte Chemie (International ed. in English) 2006; 45(32):5387–90.

11. Tuncbag N, Gursoy A, Nussinov R, Keskin O. Predicting protein-protein interactions on a proteome scale by matching evolutionary and structural similarities at interfaces using PRISM. Nature protocols 2011; 6(9):1341–54.

12. Pierce BG, Wiehe K, Hwang H, Kim B-H, Vreven T, Weng Z. ZDOCK server: interactive docking prediction of protein-protein complexes and symmetric multimers. Bioinformatics (Oxford, England) 2014; 30(12):1771–3.

13. Schneidman-Duhovny D, Inbar Y, Nussinov R, Wolfson HJ. Geometry-based flexible and symmetric protein docking. Proteins 2005; 60(2):224–31.

14. Schneidman-Duhovny D, Inbar Y, Nussinov R, Wolfson HJ. PatchDock and SymmDock: servers for rigid and symmetric docking. Nucleic acids research 2005; 33(Web Server issue):W363-7.

15. Bader B, Kuhn K, Owen DJ, Waldmann H, Wittinghofer A, Kuhlmann J. Bioorganic synthesis of lipid-modified proteins for the study of signal transduction. Nature 2000; 403(6766):223–6. Available from: URL: https://pubmed.ncbi.nlm.nih.gov/10646611/.

16. Plass T, Milles S, Koehler C, Schultz C, Lemke EA. Genetically encoded copper-free click chemistry. Angewandte Chemie (International ed. in English) 2011; 50(17):3878–81.

17. Nguyen DP, Lusic H, Neumann H, Kapadnis PB, Deiters A, Chin JW. Genetic encoding and labeling of aliphatic azides and alkynes in recombinant proteins via a pyrrolysyl-tRNA Synthetase/tRNA(CUA) pair and click chemistry. Journal of the American Chemical Society 2009; 131(25):8720–1. Available from: URL: https://pubmed.ncbi.nlm.nih.gov/19514718/.

18. Brunsveld L, Kuhlmann J, Alexandrov K, Wittinghofer A, Goody RS, Waldmann H. Lipidated ras and rab peptides and proteins--synthesis, structure, and function. Angewandte Chemie (International ed. in English) 2006; 45(40):6622–46.

19. Rostovtsev VV, Green LG, Fokin VV, Sharpless KB. A Stepwise Huisgen Cycloaddition Process: Copper(I)-Catalyzed Regioselective "Ligation" of Azides and Terminal Alkynes. Angew. Chem. Int. Ed. 2002; 41(14):2596–9.

20. Shao C, Wang X, Xu J, Zhao J, Zhang Q, Hu Y. Carboxylic acid-promoted copper(I)-catalyzed azide-alkyne cycloaddition. The Journal of organic chemistry 2010; 75(20):7002–5.

21. Hagelueken G, Ward R, Naismith JH, Schiemann O. MtsslWizard: In Silico Spin-Labeling and Generation of Distance Distributions in PyMOL. Applied magnetic resonance 2012; 42(3):377–91.

22. Abraham MJ, Murtola T, Schulz R, Páll S, Smith JC, Hess B et al. GROMACS: High performance molecular simulations through multi-level parallelism from laptops to supercomputers. SoftwareX 2015; 1-2:19–25. Available from: URL: http://www.sciencedirect.com/science/article/pii/S2352711015000059.

23. Rudack T, Xia F, Schlitter J, Kötting C, Gerwert K. The role of magnesium for geometry and charge in GTP hydrolysis, revealed by quantum mechanics/molecular mechanics simulations. Biophys J 2012; 103(2):293–302.

24. Ulmschneider JP, Ulmschneider MB. United Atom Lipid Parameters for Combination with the Optimized Potentials for Liquid Simulations All-Atom Force Field. Journal of chemical theory and computation 2009; 5(7):1803–13.

25. Jeschke G, Polyhach Y. Distance measurements on spin-labelled biomacromolecules by pulsed electron paramagnetic resonance. Physical chemistry chemical physics : PCCP 2007; 9(16):1895–910. Available from: URL: https://pubmed.ncbi.nlm.nih.gov/17431518/.

26. Pannier M, Veit S, Godt A, Jeschke G, Spiess HW. Dead-time free measurement of dipole-dipole interactions between electron spins. Journal of magnetic resonance (San Diego, Calif. : 1997) 2000; 142(2):331–40.

27. Jeschke G, Chechik V, Ionita P, Godt A, Zimmermann H, Banham J et al. DeerAnalysis2006—a comprehensive software package for analyzing pulsed ELDOR data. Appl. Magn. Reson. 2006; 30(3-4):473–98.

28. Krieger E, Koraimann G, Vriend G. Increasing the precision of comparative models with YASARA NOVA--a self-parameterizing force field. Proteins 2002; 47(3):393–402. Available from: URL: https://pubmed.ncbi.nlm.nih.gov/11948792/.